Prematurity Insults Remodel Cerebellar Development and Behavior

Georgios Sanidas[1,2] **, Gabriele Simonti[1,2]**, Javid Ghaemmaghami[3], Kyla Woyshner[4], Nora Wolff[1,2], Chad Byrd[1,2], Maria Triantafyllou[1,2], Courtney Lowe[1], Henry Salisbury[5], Evan Goldstein[6], Aaron Sathyanesan[5], Robinson Vidva[1], Ioannis Koutroulis[1,2], Genevieve Stein-O'Brien[4], Dimitrios N Sidiropoulos[4], Vittorio Gallo[7,8]* and Panagiotis Kratimenos[1,2]*

[1]Children's National Research Institute, Children's National Hospital, Washington, DC, USA
[2]Department of Pediatrics, The George Washington University School of Medicine and Health Sciences, Washington, DC, USA
[3]Department of Computational Medicine & Bioinformatics, University of Michigan, Ann Arbor, MI, USA
[4]Johns Hopkins University School of Medicine, Baltimore, MD, USA
[5]University of Dayton, Dayton, OH, USA
[6]Departments of Biological Sciences and Neuroscience & Regenerative Medicine, Augusta University, GA, USA
[7]Seattle Children's Research Institute, Seattle, WA, USA
[8]Department of Pediatrics, University of Washington School of Medicine, Seattle, WA, USA

**Equal contribution
*Corresponding Authors:
Panagiotis Kratimenos, MD, PhD
Children's National Hospital
George Washington University School of Medicine
pankratimenos@gwu.edu

Vittorio Gallo, PhD
Seattle Children's
University of Washington School of Medicine
vittorio.gallo@seattlechildrens.org

Lead contact:
Panagiotis Kratimenos, MD, PhD
Children's National Hospital
George Washington University School of Medicine
pankratimenos@gwu.edu

Abstract

Preterm survivors often develop motor and socio-cognitive impairments, yet mechanisms remain limited because prematurity arises from diverse combinations of perinatal insults. Here, we use a mouse model with experiment-controlled timing and sequence of maternal immune activation (MIA) and neonatal hypoxia (Hx), two of the most consequential prematurity-associated insults. We show that these insults remodel the developing cerebellum through distinct processes. Hx arrests granule cell maturation and reduces presynaptic excitatory input to Purkinje cells, whereas MIA perturbs granule cell migration and Purkinje dendritic development. Sequential MIA followed by Hx results in progressive neuronal mitochondrial damage and a reprogrammed circuit state. Behavioral phenotyping links these circuit states to alterations in motor-learning and coordination, translating into divergent sensorimotor organization during social investigation. These results identify developmental sequencing following preterm-birth insults as a determinant of cerebellar resilience, providing a mechanistic framework for heterogeneity in neurodevelopmental outcomes after preterm birth.

Keywords: Maternal immune activation, hypoxia, cerebellum, ASD, human, locomotor, social, behavior, spatial transcriptomics.

Introduction

Despite major advances in neonatal intensive care that have improved survival among extremely preterm infants (<28 weeks' gestation)[1,2,3], neurocognitive outcomes have plateaued[3]. Preterm birth exposes the developing brain to a constellation of biologically active insults that disrupt key neurodevelopmental processes[4,5]. Among the most prevalent prenatal contributors is MIA, which is implicated in a large fraction of preterm births associated with intrauterine infection or inflammation[6]. MIA perturbs the tightly regulated immune environment required to maintain pregnancy and disrupts fetal neurodevelopmental programs[7,8,9], increasing vulnerability to later socioemotional and cognitive impairments[10,11].

Postnatally, hypoxic exposure is one of the most frequent and consequential insults in prematurity[12]. Lung immaturity often necessitates prolonged ventilatory support[13], and early-life hypoxia disrupts neuronal differentiation, synaptogenesis, and myelination, resulting in long-term behavioral deficits[14]. However, the impact of sequential exposure to MIA and hypoxia remains poorly defined. Because prematurity is inherently heterogeneous, infants experience different combinations, severities, and timings of insults. This variability likely contributes to the wide range of neurobehavioral outcomes observed among preterm survivors[15].

The cerebellum is particularly vulnerable in this context. Its abrupt transition to the *ex-utero* environment during a critical window of maturation increases sensitivity to inflammatory and hypoxic stressors that can alter structural integrity, circuit formation, and long-range connectivity [16]. Disruption of these developmental processes has functional consequences that extend beyond

motor control, with cerebellar dysfunction implicated in ataxia as well as socioemotional and cognitive disturbances[2] and increasingly linked to neurodevelopmental conditions, such as autism spectrum disorder[17,18]. Yet the mechanistic interplay between prematurity-related insults and cerebellar development remains incompletely understood.

We hypothesized that MIA and hypoxia exert distinct and potentially sequential effects on cerebellar development, shaping both motor-learning and social behavior. To test this, we used an experimental model that enables controlled comparisons of isolated and sequential insults, coupled with comprehensive behavioral profiling to quantify locomotor learning, coordination, and socio-behavioral phenotypes. To establish translational relevance, we compared these findings with human preterm postmortem cerebellum to determine whether conserved cellular and molecular injury signatures emerge.

To investigate how MIA and hypoxia disrupt cerebellar circuit formation, we applied spatial transcriptomics across the developing cerebellar cortex, integrating transcriptional profiles with cytoarchitectural mapping during postnatal maturation. Histological analyses and cell-cycle profiling delineated insult-specific effects on progenitor maturation and laminar organization. By linking these cellular and molecular signatures to behavioral outcomes, we sought to identify mechanistic pathways through which prematurity-related insults reshape cerebellar architecture and contribute to long-term neurodevelopmental morbidity.

Results

Experimental Design of Sequential Prematurity-Associated Insults

To test how prematurity-related insults shape long-term neurobehavioral outcomes, we used an experimental mouse model that allows controlled comparison of isolated and sequential exposures. Because spontaneous preterm labor in humans is frequently triggered by intrauterine bacterial infection[19,20], prenatal MIA was induced using lipopolysaccharide (LPS), a Toll-like receptor 4 agonist that recapitulates bacterially driven inflammatory signaling[21,22]. LPS was administered during pregnancy to induce spontaneous preterm birth, targeting a developmental stage that aligns with the extreme preterm period in humans[23,24,25]. Complete methodological details, including timing, exposure parameters, and cross-species developmental alignment, are provided in the Methods.

We modeled respiratory insufficiency to mimic preterm pulmonary immaturity using a validated sublethal neonatal hypoxia paradigm[26,27,28]. Pups were exposed to chronic hypoxia across the first postnatal week, approximating the cumulative hypoxic burden experienced by extremely preterm infants in the NICU[29]. Long-term functional outcomes were evaluated through motor- and socio- behavioral testing in adulthood **(Fig. 1A)**.

This framework generated four groups that permitted direct comparison across insult conditions: saline-normoxia controls (Sal-N), isolated MIA (LPS-N), isolated hypoxia (Sal-Hx), and sequential exposure (LPS-Hx). This design enabled direct comparison of insult-specific effects

and assessment of how prenatal inflammation modifies cerebellar vulnerability to subsequent hypoxia.

Prematurity-Associated Insults Differentially Disrupt Cerebellar Motor-Learning and Coordination

Preterm-born children commonly exhibit ataxia and impaired coordination, pointing to persistent cerebellar dysfunction[30]. To determine how prematurity-related insults shape cerebellar-dependent behavior, we used the Erasmus Ladder, a high-resolution assay of locomotor learning, adaptive timing, and gait precision[31,32,33] **(Fig. 1B**).

Both MIA and hypoxia disrupted cerebellar-dependent learning. Exposure to either insult alone, MIA (LPS-N) or hypoxia (Sal-Hx), caused pronounced delays in obstacle response time compared to control, indicating impaired associative learning and adaptive timing. Sequential exposure (LPS-Hx) elicited the largest delay, consistent with cumulative effects on cerebellar learning functions **(Fig. 1C, Fig. S1A)**.

In the domain of motor coordination, reflected by misstep frequency **(Fig. 1D)**, hypoxia alone exerted a pronounced and selective deficit in motor execution and gait stability. The Sal-Hx mice displayed a threefold increase in missteps relative to all other groups, including those exposed to both insults **(Fig. 1D, Fig. S1B)**, suggesting that sequential MIA and hypoxia do not fully produce overlapping dysfunction in every cerebellar functional domain.

Collectively, these results reveal differential functional signatures of prematurity-related insults: hypoxia alone selectively impairs executional precision, while associative learning deficits are exacerbated when MIA precedes hypoxia. Sequential exposure produces a broadened,

compounded motor-learning phenotype and underscores the vulnerability of cerebellar circuits to convergent prematurity-associated insults.

Sequential MIA and Hx Recapitulate Signatures of The Preterm Human Cerebellum

To link prematurity-related motor deficits to cerebellar pathology, we performed histological analyses in the mouse model to identify cytoarchitectural changes induced by MIA and hypoxia and then compared these alterations with those observed in the preterm human cerebellum.

In mice, Purkinje cell density was transiently reduced in early-life but normalized by adulthood **(Fig. 2A-B)**. By contrast, granule cell (GC) lineage disruption emerged as a robust and persistent phenotype. External granule layer (EGL) thickness was increased across all insult groups, most prominently following MIA exposure (LPS-N and LPS-Hx), indicating delayed GC progenitor maturation **(Fig. 2C)**. Hypoxia exposure (Sal-Hx and LPS-Hx) selectively impacted mature GC by reducing their density within the internal granule layer (IGL) **(Fig. 2D)**. These findings suggest that MIA primarily impairs GC precursor maturation, while hypoxia preferentially injures postmitotic mature GCs.

Human preterm cerebella showed a parallel phenotype, with persistent and thickened EGL and reduced GC density in the IGL **(Fig. 2F-K)**, features recapitulated by both MIA and Hx in mice. Thus, both insults converge on a common vulnerability in the GC lineage that parallels preterm human cerebellar pathology.

To determine whether these cellular phenotypes reflect conserved molecular programs, we compared transcriptomes from P11 mouse cerebella across insult conditions with those from preterm versus term human cerebella. Across all comparisons, each of the prematurity-related

insults (MIA, Hx, or sequential MIA followed by Hx) generated sets of dysregulated genes that overlapped with the preterm human cerebellum, indicating that the human preterm phenotype does not arise from a single pathway but instead reflects the combined and heterogeneous effects of different prematurity insults. Each insult comparison yielded approximately 15-20% of the human preterm molecular phenotype's shared genes, with shared transcripts enriched for neurodevelopmental and circuit assembly programs: axonogenesis, neuronal differentiation, neurotransmitter signaling, and extracellular matrix remodeling (**Fig. S2**; **Tables 1-3**). These data demonstrate that prematurity insults recapitulate structural and transcriptional signatures of preterm human cerebellum, supporting the notion that the end phenotype reflects convergence of multiple prematurity-related exposures.

MIA- and Hypoxia-Driven Spatial Molecular Programs Shape the Adult Cerebellar Transcriptome

To determine how early-life perturbations reflect on adult cerebellar cortex molecular programs, we employed spatial transcriptomics (Visium) at P45 to map lasting gene expression changes within the native laminar architecture, thereby enabling us to identify persistent cell-level alterations. Using Coordinate Gene Activity in Pattern Set (CoGAPS), an unsupervised framework for identifying coordinated gene activity patterns **(Fig. 3A)**, we decomposed the cerebellar transcriptome into 13 biologically distinct M (mouse)-patterns representing cell- **(Fig. S3)** and insult-specific **(Fig. 3C)** gene expression modules.

We focused on the M-patterns most strongly associated with each insult to define how the exposures engage coordinated cell-type- and spatially organized transcriptional programs. Patterns M-1 and M-4 emerged as the dominant patterns distinguishing insult exposures **(Fig.**

3C). M-1, strongly associated with hypoxia, displayed marked spatial enrichment and comprised gene programs governing synaptic structure, vesicle trafficking, and neurotransmission **(Fig. 3D)**. In contrast, M-4, preferentially activated by MIA, exhibited the highest positive correlation with PCs **(Fig. 3B, Fig. S3)** and was defined by metabolic and mitochondrial gene programs **(Fig. 3D)**.

The correlation of pattern M-4 with MIA and its enrichment with aerobic metabolism signatures prompted us to test whether early immune exposure creates an energetic vulnerability in the cerebellum. We therefore next aimed to assess metabolic function and mitochondrial ultrastructure across insults to define early and long-term consequences.

MIA Primes the Cerebellum for Hypoxia-Driven, Progressive Mitochondrial Failure

MIA induced a cerebellar transcriptional program (pattern M-4) that is strongly enriched for regulators of oxidative metabolism and mitochondrial control **(Fig. 3D)**, implicating the mitochondrion as an early target of prenatal immune activation. This prompted asking whether this signature marks a durable, energetic failure rather than a transient stress response.

Across developmental stages, the insults diverged sharply. Hypoxia alone produced a neonatal energy deficit that was at least partially reversed by adulthood **(Fig. 4A-O)**. In contrast, MIA followed by hypoxia converted an initially compensated state into a progressive energetic failure, fully established by P45 **(Fig. 4A-O)**. Thus, what begins as a subtle metabolic disturbance after MIA, evolves into a progressive collapse of cerebellar energy support.

Multi-scale readouts, such as Seahorse Bioenergetic analysis on intact cerebellar tissue, aligned with this trajectory. At early time points (P11), cerebellar bioenergetics remained preserved, yet

by adulthood (P45) LPS-Hx animals showed apparent mitochondrial inefficiency, with increased proton leak and reduced coupling capacity, consistent with impaired oxidative phosphorylation **(Fig. 4A-C)**. Electron microscopy analysis revealed the structural correlate of this failure: while neonatal GCs and PCs retained largely intact mitochondria, adult LPS-Hx cerebella displayed reduced mitochondrial density and increased surface area, indicative of vacuolization/swelling, in both cell types **(Fig. 4E-H, 4I-L)**.

Qualitative analysis[34] further confirmed a progressive accumulation of swollen, vacuolated mitochondria with severely disorganized cristae in the LPS-Hx, whereas hypoxia-only mice resolved early abnormalities and restored a predominantly healthy mitochondrial profile by P45 **(Fig. 4M-O)**.

Together, these data support a unified model in which prenatal MIA does not perturb mitochondrial function acutely but primes the cerebellum for a progressive mitochondrial failure that is unmasked over development and amplified by later hypoxia. In contrast, hypoxia in the absence of MIA elicits reversible metabolic stress. Prematurity-associated immune activation emerges as a key driver that converts an otherwise recoverable insult into a chronic, worsening cerebellar energy-metabolic deficit.

MIA Reprograms Cerebellar Development and Redirects Hypoxia-Driven Connectivity

Persistent mitochondrial dysfunction activates checkpoint pathways that regulate neuronal proliferation and differentiation[35]. This suggests that disrupted energy homeostasis may alter cell-cycle progression, raising the question of whether neonatal insult-induced energy failure translates into changes in cell-cycle dynamics and ultimately affects GC and PC maturation **(Fig. 2).**

Using Visium-based Tricycle analysis at P45 to spatially resolve cell-cycle phase across cerebellar layers **(Fig. 5A)**, we found that neonatal hypoxia alone (Sal-Hx) was associated with a near-complete loss of the G2/M phase and marked G1/S-phase accumulation in granule cells, suggesting a persistent impairment of cell-cycle progression in adulthood. G2/M in granule cells was also reduced in LPS-N and LPS-Hx groups, further suggesting dysregulation at DNA checkpoints **(Fig. 5B)**. In PCs, no distinct pattern emerged across insult conditions **(Fig. 5B)**, consistent with the absence of measurable cellular alterations in this population at P45.

To determine whether these P45 cell-cycle abnormalities originate during the neonatal period of granule cell development, we examined checkpoint regulation at P11, when granule cell progenitors are actively proliferating within the EGL. At this stage, expression of the cell-cycle inhibitors p21 and p27 was markedly elevated in LPS-Hx cerebella compared with all other groups. **(Fig. 5C-D)**, with p21 enriched in the outer proliferative EGL and p27 in the inner EGL and emerging IGL. This pattern indicates that sequential exposure activates checkpoint arrest across the whole GC maturational trajectory.

Given the pronounced cell-cycle dysregulation and the hypoxia-associated transcriptional program (pattern M-1) enriched for synaptic and connectivity pathways, we next asked whether failure to properly exit the cell-cycle and mature into post-mitotic granule neurons compromises cell-cell interaction, the basis of circuit formation. To test whether disrupted granule cell maturation is accompanied by altered signaling with Purkinje cells, we applied the Ligand-Receptor Analysis Framework (LIANA) to the Visium dataset **(Fig. S4A-D)**. This analysis enabled joint evaluation of interaction specificity (circle presence and size) and expression magnitude (color intensity) between GCs and PCs.

Hx alone produced a marked reduction in both the specificity and strength of GC-GC and GC-PC interactions **(Fig. S4B)**. The affected pathways were enriched for glutamatergic receptor interactions, axon guidance, and cell-adhesion, programs critical for synapse formation and maintenance **(Fig. S4B)**.

In contrast, MIA alone exhibited enhanced interaction specificity in both GC and PC populations across the top expressed pathways **(Fig. S4C).** The sequential MIA and hypoxia condition (LPS-Hx) retained a PC connectivity profile similar to MIA but showed reduced and less specific GC interactions **(Fig. S4D)**. The differentially disrupted GC- and PC-interaction profiles in each insult group along with cell-cycle arrest suggested distinct connectivity alterations of the cerebellar cortex in the presence of each insult. To address this, we performed presynaptic vGLUT2+ immunostaining along with PC structural dendritic analysis **(Fig. 6A-B)**. Across conditions, presynaptic afferent input, indexed by vGLUT2^{+} puncta, and postsynaptic Purkinje cell dendritic architecture were differentially affected, revealing insult-specific mechanisms of circuit remodeling.

Hypoxia alone primarily disrupted presynaptic connectivity. Despite preserved PC dendritic length and complexity (**Fig. 6C-E**), Sal-Hx mice exhibited near-complete depletion of vGLUT2+ presynaptic afferent input (**Fig. 6A-B**), indicating that PCs remain structurally intact yet functionally disconnected. This pattern aligns with the marked reduction in mature granule cells in this group and identifies synaptic input loss as the dominant cellular mechanism of hypoxia-induced circuit dysfunction.

In contrast, MIA selectively impaired postsynaptic structure. MIA-exposed groups (LPS-N and LPS-Hx) showed significantly reduced PC dendritic length and complexity relative to controls

(**Fig. 6D-E**), while presynaptic vGLUT2+ input was preserved or increased (**Fig. 6A-B**). This mismatch suggests that intact afferent projections converge onto a reduced postsynaptic territory, altering synaptic integration without eliminating inputs.

Sequential exposure (LPS-Hx) produced a reconfigured connectivity state that was not additive. Rather than exacerbating synaptic loss, prior MIA reshaped the hypoxic response, yielding reduced dendritic complexity and a redistribution of vGLUT2^{+} puncta toward distal dendritic compartments, rather than global afferent depletion (**Fig. 6A-E**).

These data show that prematurity-related insults disrupt cerebellar circuit assembly through distinct, developmentally constrained mechanisms. Hypoxia drives sustained granule cell-cycle arrest, leading to loss of presynaptic input and functional disconnection despite preserved Purkinje cell morphology, whereas MIA restricts dendritic growth while maintaining afferent projections, altering synaptic integration. Sequential exposure reprograms the hypoxic response, producing redistributed synaptic input onto a reduced dendritic scaffold, rather than global synaptic loss. Together, these circuit configurations link early cell-cycle disruption to persistent alterations in cerebellar network organization with implications for motor and socio-cognitive output.

Sequential Insults Transform Hypoxia-Induced Social and Motor Dysregulation

Differences in presynaptic afferent input and postsynaptic cerebellar architecture across groups **(Fig. 6)**, together with motor-cognitive and coordination deficits **(Fig. 1)**, indicate disrupted cerebellar integration of sensory-feedback and motor responses, key integrative functions supporting social behavior. We therefore quantified both overall social preference and the kinematic structure of locomotor and investigatory behavior during the three-chamber assay.

Using grid-based mapping and DeepLabCut tracking to measure social exploration[36,37] **(Fig. 7A-B, Fig. S5A-C)**, we found that single-insult exposure significantly reduced social preference.

Both MIA alone (LPS-N) and hypoxia alone (Sal-Hx) mice spent comparable time in the presence of a conspecific stranger and in non-social grid zones, consistent with impaired sociability arising through distinct contributing mechanisms. Conversely, sequentially exposed LPS-Hx animals showed social interaction times more aligned with controls, suggesting partial preservation of gross social preference despite persistent circuit disruption (**Fig. 7C**).

However, aggregate sociability measures alone could not distinguish intact exploratory capacity from impaired engagement driven by sensory-feedback deficits. To address this, we repurposed the habituation phase of the three-chamber assay as a controlled open-field environment, enabling quantification of exploratory behavior within the same spatial context later used for social interaction. Assessing stimulus-free locomotion in the social arena minimized confounds from novelty or context switching and allowed direct comparison between each animal's intrinsic exploratory behavior and its subsequent social responses.

This analysis revealed a qualitatively different exploratory phenotype in the hypoxic groups, particularly in LPS-Hx mice: prolonged immobility, corner dwelling, and marked reductions in open-field exploration **(Fig. 7D-E)**. Thus, combined exposure did not restore normal exploratory drive; instead, it imposed a constrained baseline locomotor strategy that can mask underlying circuit dysfunction when behavior is summarized solely by aggregate measures of social time.

To determine whether this altered stimulus-free exploratory state manifested as different motor investigatory behavior once social and novel cues were present, we used an unsupervised algorithm (B-SOiD) to segment tracked movements into unbiased kinematic motif clusters (**Fig. 8A-C, Table 4, Fig. S6**). Hx-only mice showed a predominance of repetitive head and body turning (clusters 1 and 12) and reduced use of interactive clusters (7 and 8), consistent with stereotyped, inflexible movement patterns that limit normal social investigation **(Fig. 8D)**.

In contrast, LPS-Hx mice displayed a hyper-interactive pattern of social investigation, marked by frequent approach bouts and persistent upright postures, preferentially expressed in the stranger mouse chamber (cluster 8; **Fig. 8D-E, Fig. S6**). These exaggerated and repetitive behaviors diverged from both control and single-insult groups, indicating dysregulated, not restored, social engagement.

Collectively, these results provide a behavioral readout of insult-specific cerebellar circuit remodeling. In hypoxia-exposed mice, loss of vGLUT2^{+} afferent input aligns with impaired motor coordination and a shift toward rigid, stereotyped locomotor motifs with reduced sensory-guided investigation. When MIA precedes hypoxia, the resulting circuit state preserves overall social preference but reorganizes social exploration into excessive, repetitive investigatory patterns, consistent with disrupted Purkinje integration and altered timing of social-motor programs. In this framework, sequential inflammatory and hypoxic insults generate a socio-motor phenotype characterized by abnormal coupling between sensory processing, locomotor state, and social investigation, linking cerebellar connectivity disruptions to adult socio-motor dysfunction.

Discussion

This study links maternal immune activation and neonatal hypoxia, two major prematurity-associated insults, to distinct yet converging disruptions in cerebellar development that shape long-term motor and social outcomes. Through integrated behavioral, anatomical, and spatial transcriptomic analyses across mouse and human tissue, we demonstrate that prematurity-associated insults recapitulate key features of the preterm cerebellum, with sequential exposure most closely mirroring the cytoarchitectural and molecular signatures observed in human postmortem tissue. Although prematurity is a leading cause of neurodevelopmental disability[38], its associated insults are often examined in isolation. Here, single and sequential-insult exposure highlights vulnerable pathways in circuit assembly, synaptic organization, and metabolic regulation.

A central insight is that MIA and hypoxia perturb cerebellar circuitry by acting on distinct developmental vulnerabilities, with MIA modifying the cerebellar response to subsequent hypoxic exposure. Hypoxia primarily compromises presynaptic granule cell input, whereas MIA disrupts postsynaptic Purkinje cell maturation while preserving afferent connectivity. When MIA precedes hypoxia, delayed GC maturation shifts the window of hypoxic susceptibility, attenuating acute synaptic loss but yielding an immature and disorganized circuit state. This developmental reprogramming has clear behavioral consequences, including altered sociability and motor-cognitive impairment. More broadly, these findings provide a mechanistic framework for the heterogeneity observed among preterm infants with similar clinical exposures [15,3] and underscore the importance of developmental timing in shaping cerebellar vulnerability and long-

term outcome[16], arguing for temporally resolved frameworks of prematurity rather than static exposure-based models.

Moreover, the dissociation between motor and social outcomes raises important questions about cerebellar contributions to non-motor behavior. The cerebellum is increasingly recognized as a node in circuits supporting social cognition[17,18] yet the mechanisms linking cerebellar injury to social deficits remain unclear[39,40]. In this study, the kinematic differences observed across single- and sequential-insult conditions likely reflect differential effects of early-life injury on cerebellar error-correction processes. Cerebellar learning depends on the integration of sensory prediction errors with contextual information conveyed by afferent inputs to PCs, including GC and climbing fiber signaling, to guide adaptive updating of motor behavior[41,42]. This integrative process requires intact PC dendritic architecture to support learning-related signaling[43].

Our findings indicate that MIA, hypoxia, and their sequential combination perturb cerebellar error-integration through distinct developmental constraints: MIA limits dendritic maturation, whereas hypoxia compromises the afferent contextual input required to interpret error signals. When combined, these insults yield a circuit in which error signals are generated but inefficiently integrated, resulting in maladaptive social-exploratory strategies. Importantly, this framework suggests that behavioral abnormalities arise from altered cerebellar computation rather than irreversible motor failure[44], raising the possibility that interventions aimed at restoring dendritic integration, afferent signaling, or their coordination could partially normalize circuit function. Such strategies may hold potential not only for correcting motor deficits but also for improving higher-order behavioral outcomes by re-establishing adaptive cerebellar error processing[45].

Beyond altered connectivity, our findings identify progressive mitochondrial failure as another major mechanism linking early-life insults to lasting cerebellar dysfunction. In the sequential exposure group, an initial phase of metabolic compensation was followed by delayed bioenergetic collapse, indicating that MIA establishes a mitochondrial priming state that heightens vulnerability to later hypoxic stress. This inflammatory priming suggests that early immune activation sensitizes developing neurons to subsequent metabolic challenges, offering a potential explanation for the prolonged vulnerability seen in preterm infants beyond the immediate perinatal period[6,12]. Together with the connectivity changes, these findings highlight multiple, interacting pathways through which early-life insults shape long-term cerebellar function. The identification of a primed mitochondrial state suggests opportunities for targeted metabolic strategies[46] with potential relevance for mitigating prematurity-associated neurological vulnerability.

This work has limitations inherent to developmental modeling. Mouse systems cannot fully recapitulate the prolonged and heterogeneous neonatal intensive care unit (NICU) experience[47], nor the complex mixture of nutritional, pharmacologic, socioeconomic, and environmental exposures that shape the human preterm brain[2,48]. Spatial transcriptomics provide anatomically anchored molecular snapshots but not continuous trajectories of gene expression change. Definitive causal links between specific spatial gene programs and discrete behaviors will require cell-type-specific manipulations across tightly defined developmental windows. Nonetheless, this model uniquely allows controlled sequencing of insults within a conserved cerebellar architecture, a level of experimental resolution that purely human studies cannot achieve.

In summary, these findings demonstrate that prematurity-associated cerebellar injury is governed by developmental timing and the interaction of early-life insults. MIA reshapes maturational and metabolic states, thereby modifying the cerebellar response to subsequent hypoxia at cellular and circuit levels. The cerebellum's extended postnatal development renders it particularly sensitive to exposure order[49], with granule and Purkinje cells serving as interconnected substrates of vulnerability[50]. By linking mitochondrial dysfunction, disrupted cell-cycle regulation, and altered synaptic organization to motor and social outcomes, this work provides a mechanistic framework for the heterogeneous neurodevelopmental trajectories observed in preterm infants[51]. More broadly, these findings highlight the importance of incorporating developmental timing into risk stratification and suggest that effective strategies to mitigate prematurity-related brain injury should align with dynamic windows of cerebellar vulnerability.

Resource availability

Lead contact
Further information and requests for resources and reagents should be directed to and will be fulfilled by the lead contact, Panagiotis Kratimenos, M.D., Ph.D. (pankratimenos@gwu.edu, Panagiotis.Kratimenos@childrensnational.org)

Materials availability
This study did not generate new unique reagents.

Data and code availability
Bulk and spatial RNA-seq data analysis from cerebellar mouse and human tissue have been deposited in the NoCodeSeg repository and are publicly available. The accession number is listed in the methods. Any additional information required to reanalyze the data reported in this paper is available from the lead contact upon request.

Acknowledgments

This work was supported by the Raynor Cerebellum Project (P.K.), R37NS109478 (Javits Award; V.G.), K12HD001399 Child Health Research Career Development Award (CHRCDA, P.K.), American SIDS Institute (P.K.), a Children's National Board of Visitors' Grant (P.K.) and 1R21NS135088 (I.K.). This study was also supported by the District of Columbia Intellectual and Developmental Disabilities Research Center (DC-IDDRC) award P50HD105328; (V.G.) from the Eunice Kennedy Shriver National Institute of Child Health and Human Development. We thank the Neurobehavioral Evaluation Core of the Intellectual and Developmental Disabilities Research Center at Children's National Hospital for training and supervision for behavioral testing and Dr. Jacqueline Crawley of the University of California Davis MIND Institute for her assistance with manuscript preparation.

Declaration of interests

The authors declare no competing interests.

Author contributions

P.K., conceived and designed the study. G.San., G.Sim., P.K., I.K., J.G., and K.W. performed the experiments and collected the data. K.W., G.Stein., R.V., D.S., H.S., E.G. and A.S. conducted the data analysis. G.San., G.Sim., P.K., N.W., M.T., C.B., and I.K. contributed to the interpretation of the results and provided critical feedback. G.San., G.Sim., V.G. and P.K. drafted the manuscript, and all authors contributed to the revisions and approved the final version.

Supplemental information

Supplemental Figure S1-S7 with legends, Table 1-4, Supplemental Figure Files, Statistic Files.

1 Pascoe, L., Burnett, A. C. & Anderson, P. J. Cognitive and academic outcomes of children born extremely preterm. *Semin Perinatol* **45**, 151480 (2021). https://doi.org/10.1016/j.semperi.2021.151480
2 Inder, T. E., Volpe, J. J. & Anderson, P. J. Defining the Neurologic Consequences of Preterm Birth. *N Engl J Med* **389**, 441-453 (2023). https://doi.org/10.1056/NEJMra2303347
3 Cheong, J. L. Y. *et al.* Temporal Trends in Neurodevelopmental Outcomes to 2 Years After Extremely Preterm Birth. *JAMA Pediatr* **175**, 1035-1042 (2021). https://doi.org/10.1001/jamapediatrics.2021.2052
4 Twilhaar, E. S. *et al.* Cognitive Outcomes of Children Born Extremely or Very Preterm Since the 1990s and Associated Risk Factors: A Meta-analysis and Meta-regression. *JAMA Pediatr* **172**, 361-367 (2018). https://doi.org/10.1001/jamapediatrics.2017.5323
5 Kratimenos, P., Sanidas, G., Simonti, G., Byrd, C. & Gallo, V. The shifting landscape of the preterm brain. *Neuron* **113**, 2042-2064 (2025). https://doi.org/10.1016/j.neuron.2025.03.024
6 Romero, R. *et al.* Prevalence and clinical significance of sterile intra-amniotic inflammation in patients with preterm labor and intact membranes. *Am J Reprod Immunol* **72**, 458-474 (2014). https://doi.org/10.1111/aji.12296
7 Agrawal, V. & Hirsch, E. Intrauterine infection and preterm labor. *Semin Fetal Neonatal Med* **17**, 12-19 (2012). https://doi.org/10.1016/j.siny.2011.09.001
8 Erlebacher, A. Immunology of the maternal-fetal interface. *Annu Rev Immunol* **31**, 387-411 (2013). https://doi.org/10.1146/annurev-immunol-032712-100003
9 Lu-Culligan, A. & Iwasaki, A. The Role of Immune Factors in Shaping Fetal Neurodevelopment. *Annu Rev Cell Dev Biol* **36**, 441-468 (2020). https://doi.org/10.1146/annurev-cellbio-021120-033518
10 Pendyala, G. *et al.* Maternal Immune Activation Causes Behavioral Impairments and Altered Cerebellar Cytokine and Synaptic Protein Expression. *Neuropsychopharmacology* **42**, 1435-1446 (2017). https://doi.org/10.1038/npp.2017.7
11 Zuckerman, L. & Weiner, I. Maternal immune activation leads to behavioral and pharmacological changes in the adult offspring. *J Psychiatr Res* **39**, 311-323 (2005). https://doi.org/10.1016/j.jpsychires.2004.08.008
12 Salmaso, N., Jablonska, B., Scafidi, J., Vaccarino, F. M. & Gallo, V. Neurobiology of premature brain injury. *Nat Neurosci* **17**, 341-346 (2014). https://doi.org/10.1038/nn.3604
13 Norman, M., Jonsson, B., Wallstrom, L. & Sindelar, R. Respiratory support of infants born at 22-24 weeks of gestational age. *Semin Fetal Neonatal Med* **27**, 101328 (2022). https://doi.org/10.1016/j.siny.2022.101328
14 Sathyanesan, A., Kundu, S., Abbah, J. & Gallo, V. Neonatal brain injury causes cerebellar learning deficits and Purkinje cell dysfunction. *Nat Commun* **9**, 3235 (2018). https://doi.org/10.1038/s41467-018-05656-w
15 Mwaniki, M. K., Atieno, M., Lawn, J. E. & Newton, C. R. Long-term neurodevelopmental outcomes after intrauterine and neonatal insults: a systematic review. *Lancet* **379**, 445-452 (2012). https://doi.org/10.1016/S0140-6736(11)61577-8

16 Volpe, J. J. Cerebellum of the premature infant: rapidly developing, vulnerable, clinically important. *J Child Neurol* **24**, 1085-1104 (2009). https://doi.org/10.1177/0883073809338067
17 Wang, L. A. L., Petrulla, V., Zampella, C. J., Waller, R. & Schultz, R. T. Gross motor impairment and its relation to social skills in autism spectrum disorder: A systematic review and two meta-analyses. *Psychol Bull* **148**, 273-300 (2022). https://doi.org/10.1037/bul0000358
18 Craig, F. *et al.* Characterization of Autism Spectrum Disorder (ASD) subtypes based on the relationship between motor skills and social communication abilities. *Hum Mov Sci* **77**, 102802 (2021). https://doi.org/10.1016/j.humov.2021.102802
19 Goldenberg, R. L., Hauth, J. C. & Andrews, W. W. Intrauterine infection and preterm delivery. *N Engl J Med* **342**, 1500-1507 (2000). https://doi.org/10.1056/NEJM200005183422007
20 Hunter, P. J. *et al.* Biological and pathological mechanisms leading to the birth of a small vulnerable newborn. *Lancet* **401**, 1720-1732 (2023). https://doi.org/10.1016/S0140-6736(23)00573-1
21 Pawelczyk, E. *et al.* Spontaneous preterm labor is associated with an increase in the proinflammatory signal transducer TLR4 receptor on maternal blood monocytes. *BMC Pregnancy Childbirth* **10**, 66 (2010). https://doi.org/10.1186/1471-2393-10-66
22 Firmal, P., Shah, V. K. & Chattopadhyay, S. Insight Into TLR4-Mediated Immunomodulation in Normal Pregnancy and Related Disorders. *Front Immunol* **11**, 807 (2020). https://doi.org/10.3389/fimmu.2020.00807
23 Rice, D. & Barone, S., Jr. Critical periods of vulnerability for the developing nervous system: evidence from humans and animal models. *Environ Health Perspect* **108 Suppl 3**, 511-533 (2000). https://doi.org/10.1289/ehp.00108s3511
24 Theiler, K. *The House Mouse*. 1 edn, (Springer Berlin, Heidelberg).
25 True, H., Blanton, M., Sureshchandra, S. & Messaoudi, I. Monocytes and macrophages in pregnancy: The good, the bad, and the ugly. *Immunol Rev* **308**, 77-92 (2022). https://doi.org/10.1111/imr.13080
26 Jablonska, B. *et al.* Sirt2 promotes white matter oligodendrogenesis during development and in models of neonatal hypoxia. *Nat Commun* **13**, 4771 (2022). https://doi.org/10.1038/s41467-022-32462-2
27 Forbes, T. A. *et al.* Environmental enrichment ameliorates perinatal brain injury and promotes functional white matter recovery. *Nat Commun* **11**, 964 (2020). https://doi.org/10.1038/s41467-020-14762-7
28 Kundu, S. *et al.* Cerebellar Purkinje Cell Activity Regulates White Matter Response and Locomotor Function after Neonatal Hypoxia. *J Neurosci* **45** (2025). https://doi.org/10.1523/JNEUROSCI.0899-24.2024
29 Hyttel-Sorensen, S. *et al.* Cerebral near infrared spectroscopy oximetry in extremely preterm infants: phase II randomised clinical trial. *BMJ* **350**, g7635 (2015). https://doi.org/10.1136/bmj.g7635
30 Albayrak, B. *et al.* Ataxia Rating Scales Reveal Increased Scores in Very Preterm Born 5-6-Year-Old Preschool Children and Young Adults. *Cerebellum* **22**, 877-887 (2023). https://doi.org/10.1007/s12311-022-01463-8

31 Sathyanesan, A., Kratimenos, P. & Gallo, V. Disruption of neonatal Purkinje cell function underlies injury-related learning deficits. *Proc Natl Acad Sci U S A* **118** (2021). https://doi.org/10.1073/pnas.2017876118
32 Sathyanesan, A. *et al.* Emerging connections between cerebellar development, behaviour and complex brain disorders. *Nat Rev Neurosci* **20**, 298-313 (2019). https://doi.org/10.1038/s41583-019-0152-2
33 Sathyanesan, A. & Gallo, V. Cerebellar contribution to locomotor behavior: A neurodevelopmental perspective. *Neurobiol Learn Mem* **165**, 106861 (2019). https://doi.org/10.1016/j.nlm.2018.04.016
34 Coughlin, L., Morrison, R. S., Horner, P. J. & Inman, D. M. Mitochondrial morphology differences and mitophagy deficit in murine glaucomatous optic nerve. *Invest Ophthalmol Vis Sci* **56**, 1437-1446 (2015). https://doi.org/10.1167/iovs.14-16126
35 Antico Arciuch, V. G., Elguero, M. E., Poderoso, J. J. & Carreras, M. C. Mitochondrial regulation of cell cycle and proliferation. *Antioxid Redox Signal* **16**, 1150-1180 (2012). https://doi.org/10.1089/ars.2011.4085
36 Yang, M., Silverman, J. L. & Crawley, J. N. Automated three-chambered social approach task for mice. *Curr Protoc Neurosci* **Chapter 8**, Unit 8 26 (2011). https://doi.org/10.1002/0471142301.ns0826s56
37 Lauer, J. *et al.* Multi-animal pose estimation, identification and tracking with DeepLabCut. *Nat Methods* **19**, 496-504 (2022). https://doi.org/10.1038/s41592-022-01443-0
38 Mitha, A. *et al.* Neurological development in children born moderately or late preterm: national cohort study. *BMJ* **384**, e075630 (2024). https://doi.org/10.1136/bmj-2023-075630
39 D'Mello, A. M. & Stoodley, C. J. Cerebro-cerebellar circuits in autism spectrum disorder. *Front Neurosci* **9**, 408 (2015). https://doi.org/10.3389/fnins.2015.00408
40 Van Overwalle, F. *et al.* Consensus Paper: Cerebellum and Social Cognition. *Cerebellum* **19**, 833-868 (2020). https://doi.org/10.1007/s12311-020-01155-1
41 Oh, J. *et al.* Incident allergic diseases in post-COVID-19 condition: multinational cohort studies from South Korea, Japan and the UK. *Nat Commun* **15**, 2830 (2024). https://doi.org/10.1038/s41467-024-47176-w
42 Suomalainen, A. Mitochondrial DNA Inheritance in Humans: Mix, Match, and Survival of the Fittest. *Cell Metab* **30**, 231-232 (2019). https://doi.org/10.1016/j.cmet.2019.07.009
43 Loughran, G. *et al.* Unusually efficient CUG initiation of an overlapping reading frame in POLG mRNA yields novel protein POLGARF. *Proc Natl Acad Sci U S A* **117**, 24936-24946 (2020). https://doi.org/10.1073/pnas.2001433117
44 Wang, S. S., Kloth, A. D. & Badura, A. The cerebellum, sensitive periods, and autism. *Neuron* **83**, 518-532 (2014). https://doi.org/10.1016/j.neuron.2014.07.016
45 Brorsen, E., Rasmussen, T. D., Ekstrom, C. T., Osborne, R. H. & Villadsen, S. F. Health literacy responsiveness: a cross-sectional study among pregnant women in Denmark. *Scand J Public Health* **50**, 507-515 (2022). https://doi.org/10.1177/14034948211004320
46 Aziz, W. *et al.* Distinct kinetics of synaptic structural plasticity, memory formation, and memory decay in massed and spaced learning. *Proc Natl Acad Sci U S A* **111**, E194-202 (2014). https://doi.org/10.1073/pnas.1303317110

47 Smith, G. C. *et al.* Neonatal intensive care unit stress is associated with brain development in preterm infants. *Ann Neurol* **70**, 541-549 (2011). https://doi.org/10.1002/ana.22545
48 Benavente-Fernandez, I., Siddiqi, A. & Miller, S. P. Socioeconomic status and brain injury in children born preterm: modifying neurodevelopmental outcome. *Pediatr Res* **87**, 391-398 (2020). https://doi.org/10.1038/s41390-019-0646-7
49 Leto, K. *et al.* Consensus Paper: Cerebellar Development. *Cerebellum* **15**, 789-828 (2016). https://doi.org/10.1007/s12311-015-0724-2
50 Wallace, R. & Mills, B. A Study of the Food Environment at Australian Family Day Care. *Nutrients* **11** (2019). https://doi.org/10.3390/nu11102395
51 Volpe, J. J. Brain injury in premature infants: a complex amalgam of destructive and developmental disturbances. *Lancet Neurol* **8**, 110-124 (2009). https://doi.org/10.1016/S1474-4422(08)70294-1

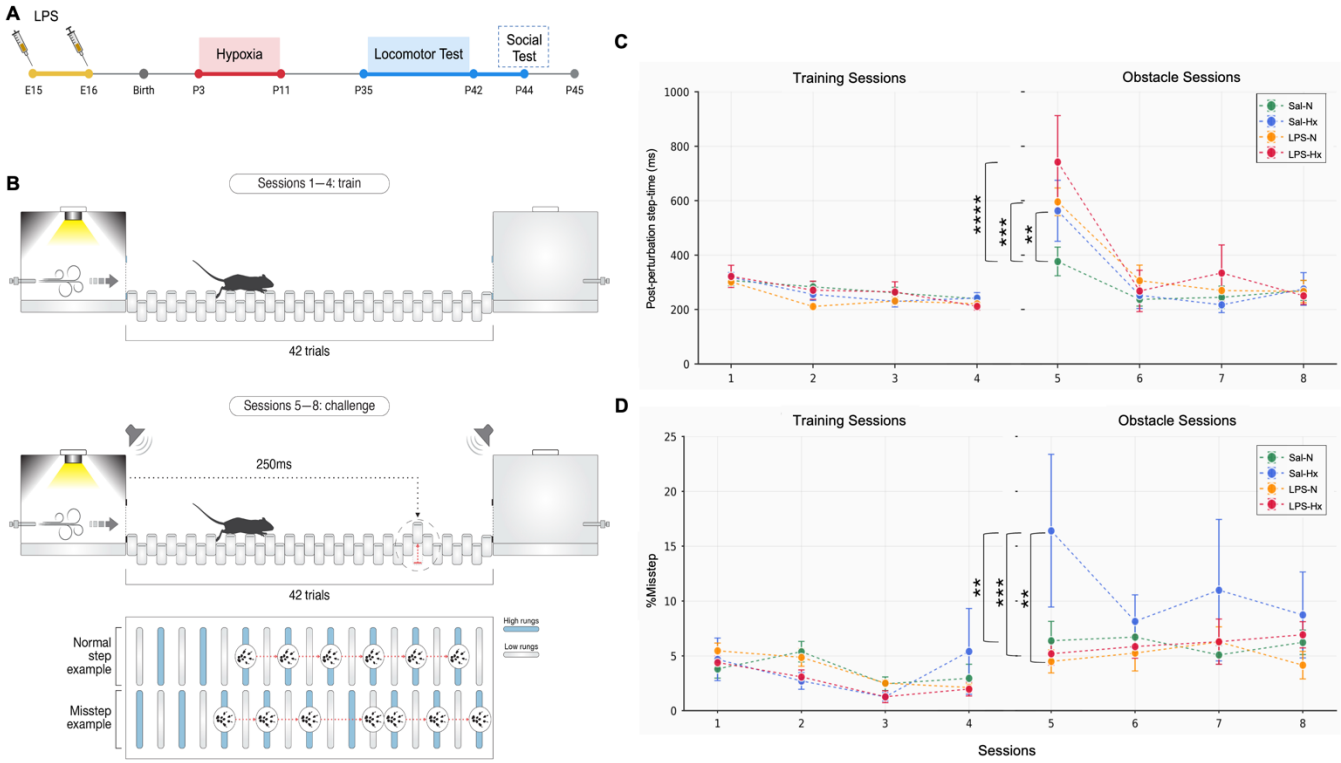

Figure 1 - Distinct Long-Term Cerebellar Motor Deficits Induced by MIA and Hx:
(A) Experimental timeline of the sequential prematurity insult mouse model. Pregnant dams received intraperitoneal injections of lipopolysaccharide (LPS) or saline (Sal) at embryonic days 15 and 16 (E15-E16) to induce maternal immune activation. Offspring were subsequently exposed to chronic hypoxia (Hx) or maintained under normoxic conditions (N) from postnatal day 3 through 11 (P3-P11). Cerebellar-dependent motor function was evaluated using the ErasmusLadder at P35-P42, followed by social behavior testing at P45. (**B)** Schematic of the

ErasmusLadder paradigm. Mice traversed a horizontal ladder from an origin box to a goal box (equivalent of one trial) over eight sessions of 42 trials each. Sessions 1-4 served as training under unperturbed conditions, whereas sessions 5-8 introduced challenge trials incorporating an auditory cue, an obstacle (raised rung), or both, presented in randomized order. Representative diagrams illustrate normal stepping patterns and missteps, defined as limb placement errors reflecting impaired motor coordination. (**C**) Post-perturbation step-time across sessions. All groups performed comparably during training sessions. Upon obstacle introduction, Sal-Hx, LPS-N, and LPS-Hx mice exhibited significantly prolonged step-times relative to Sal-N controls (Sal-N versus Sal-Hx, **P = 0.0038; Sal-N versus LPS-N, ***P = 0.0002; Sal-N versus LPS-Hx, ****P < 0.0001). (**D**) Misstep frequency across sessions. Sal-Hx mice demonstrated elevated misstep rates during obstacle sessions compared with all other groups (Sal-Hx versus Sal-N, **P = 0.0019; Sal-Hx versus LPS-N, ***P = 0.0008; Sal-Hx versus LPS-Hx, **P = 0.0019). Data are presented as mean ± SD; n = 8-18 animals per group; two-way repeated-measures ANOVA with Tukey's post hoc correction for multiple comparisons; *P < 0.05, **P < 0.01, ***P < 0.001, ****P < 0.0001. E, embryonic day; Hx, hypoxia; LPS, lipopolysaccharide; N, normoxia; P, postnatal day; Sal, saline; SD, standard deviation.

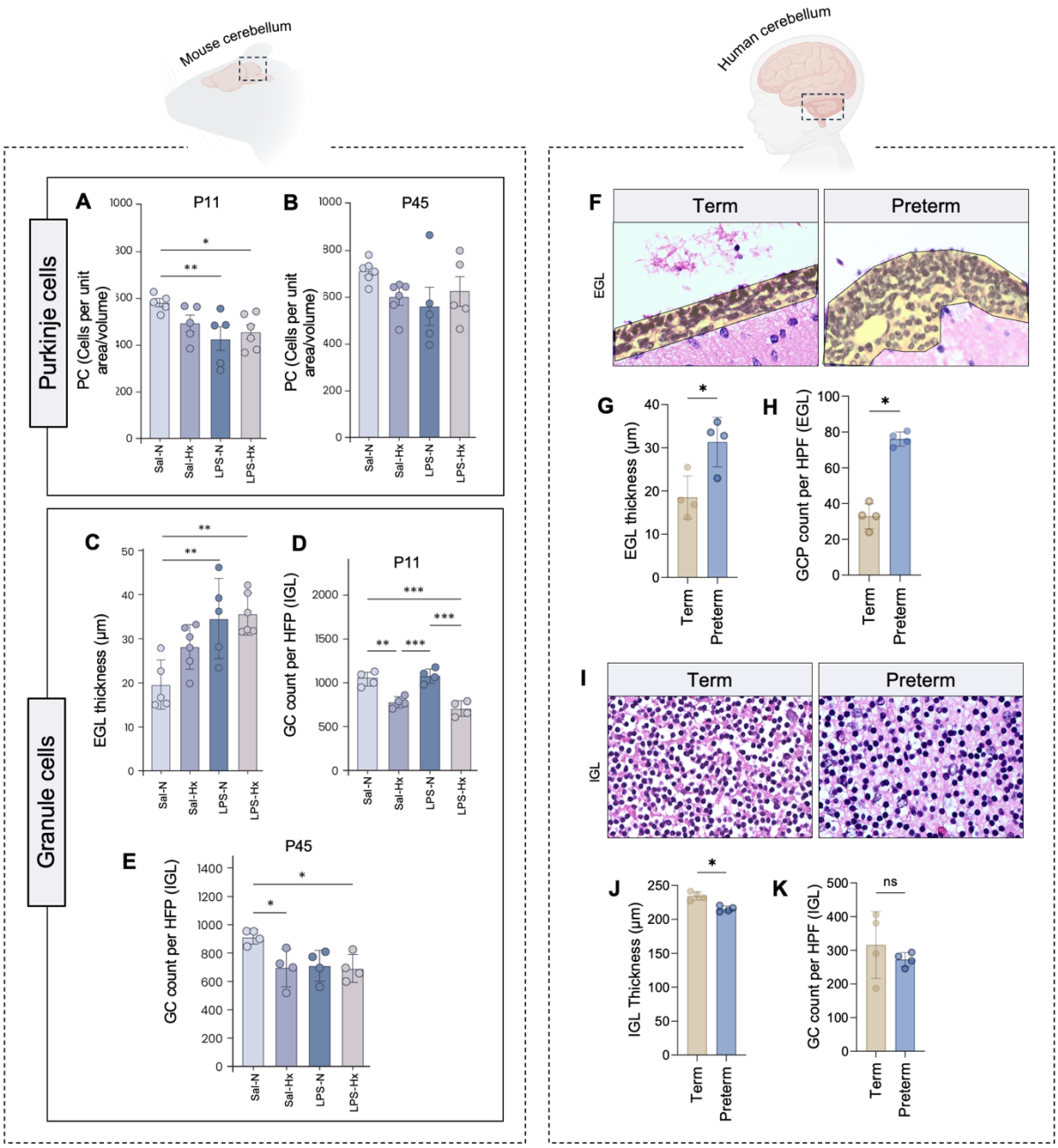

Figure 2 -Prematurity Insults Disrupt Cerebellar Cytoarchitecture and Mimic Human Preterm Pathology: (**A-E**) Histological analysis of mouse cerebellar development. Purkinje cell count (cell per unit area/volume) was quantified at P11 (**A**) and P45 (**B**). External granule layer thickness was measured at P11 (**C**), as this transient germinal zone is depleted by P20. Granule cell density within the internal granule layer was assessed at P11 (**D**) and P45 (**E**). (**F-K**) Histological analysis of human cerebellar tissue from term and preterm infants. Representative photomicrographs of the external granule layer (**F**) and internal granule layer (**I**) are shown at

40× magnification, with the external granule layer demarcated in yellow. Quantification of external granule layer thickness (**G**) and granule cell precursor counts (**H**) in term versus preterm cerebellum. Internal granule layer thickness (**J**) and granule cell density (**K**) in term versus preterm cerebellum. For mouse studies, n = 4-5 per group; one-way ANOVA with uncorrected Fisher's LSD (**A-B**) or Tukey's post hoc correction (**C-E**). For human studies, n = 4 term and n = 4 preterm subjects; unpaired two-tailed Student's t-test. Data are presented as mean ± SD; *P < 0.05, **P < 0.01, ***P < 0.001. EGL, external granule layer; GC, granule cell; GCP, granule cell precursor; H&E, hematoxylin and eosin; HPF, high-power field; Hx, hypoxia; IGL, internal granule layer; LPS, lipopolysaccharide; ML, molecular layer; N, normoxia; P, postnatal day; PC, Purkinje cell; PCL, Purkinje cell layer; Sal, saline; SD, standard deviation.

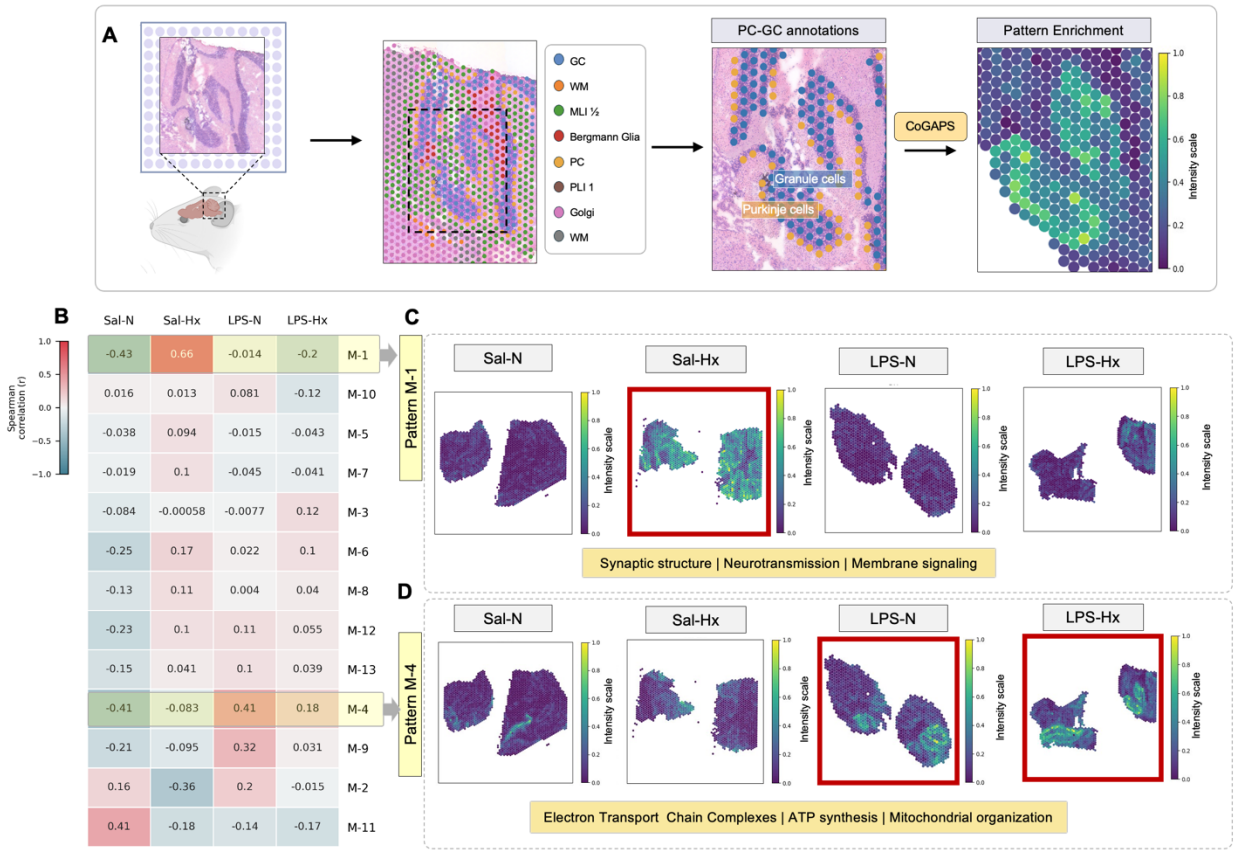

Figure 3 - Prematurity Insult-Specific Alterations in Cerebellar Development Molecular Programs: (A) Schematic illustration of the analytical pipeline for spatial transcriptomics and CoGAPS pattern discovery in mouse cerebellum. Hematoxylin and eosin-stained cerebellar

tissue sections were processed for Visium spatial transcriptomics. Representative images demonstrate cell-type annotation of cerebellar regions at 10× magnification, with granule cells (blue) and Purkinje cells (orange) identified at 40× magnification. Following CoGAPS analysis, gene expression patterns were mapped onto tissue architecture, with expression levels displayed on an intensity scale ranging from low (blue) to high (yellow). **(B)** Heatmap displaying Spearman correlation coefficients between CoGAPS-derived expression patterns and experimental conditions across all four groups. Correlation values range from high positive (red, $r = 1$) to high negative (blue, $r = -1$). **(C-D)** Spatial visualization of two representative CoGAPS patterns across experimental groups. Pattern M-1 **(C)** demonstrates enrichment for genes associated with synaptic structure, neurotransmission, and membrane signaling pathways. Pattern M-4 **(D)** demonstrates enrichment for genes associated with electron transport chain complexes, ATP synthesis, and mitochondrial organization. Expression intensity scale ranges from low (blue) to high (yellow), with condition-specific spatial distributions highlighted (red boxes). For all spatial transcriptomics analyses, n = 2 per group. CoGAPS, Coordinated Gene Activity in Pattern Sets; GC, granule cell; Hx, hypoxia; LPS, lipopolysaccharide; M, mouse; MIA, maternal immune activation; MLI, molecular layer interneuron; N, normoxia; PC, Purkinje cell; PLI, Purkinje layer interneuron; Sal, saline; WM, white matter.

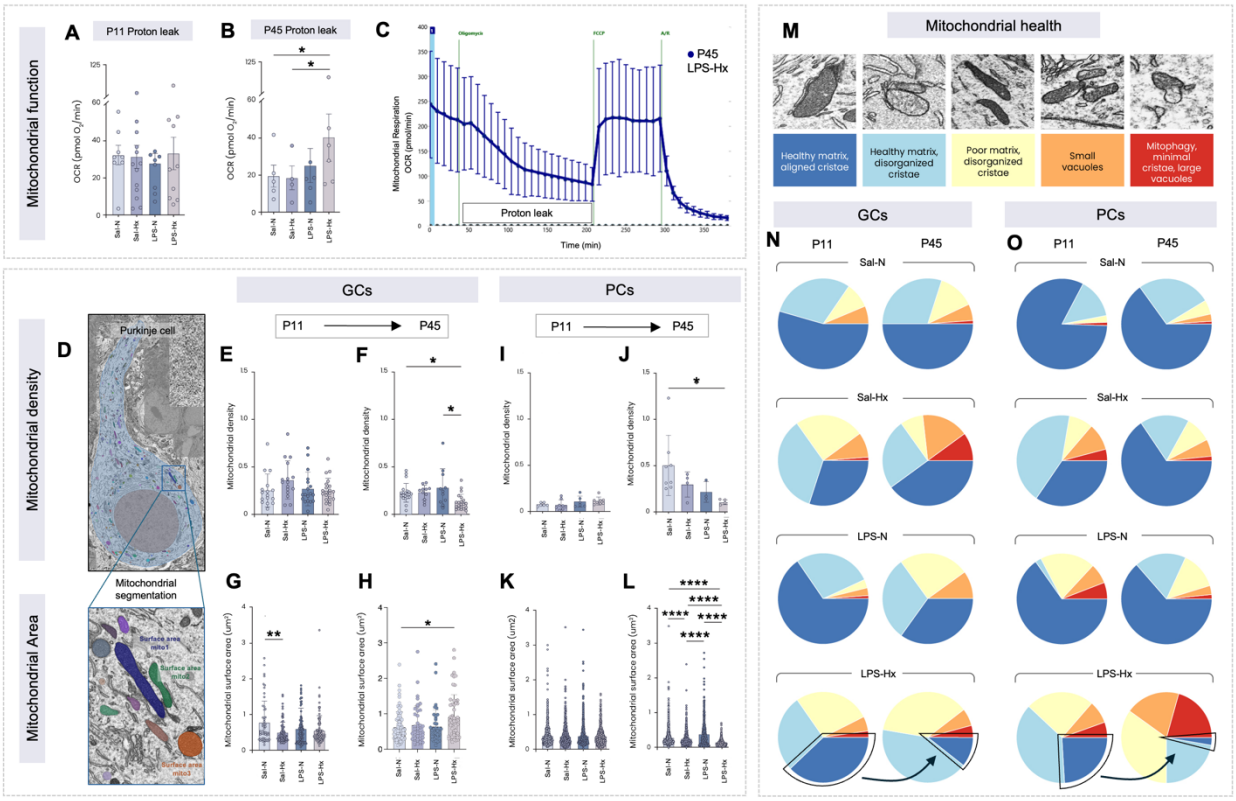

Figure 4 - MIA-Induced Metabolic Priming Increases Vulnerability to Neonatal Hypoxia: **(A-B)** Quantification of proton leak rates at P11 **(A)** and P45 **(B)** across experimental groups (LPS-Hx versus Sal-Hx, *P = 0.0281; LPS-Hx versus Sal-N, *P= 0.0484). **(C)** Representative Seahorse XF oxygen consumption rate trace from LPS-Hx cerebellum at P45, displaying mitochondrial respiration across metabolic phases following sequential machine-applied injection of oligomycin, FCCP, and antimycin A/rotenone. **(D)** Schematic illustration of electron microscopy-based mitochondrial analysis in Purkinje cells. Top panel demonstrates mitochondrial identification and segmentation within a Purkinje cell soma; bottom panel displays representative examples of individual mitochondria with corresponding surface area measurements. **(E-H)** Mitochondrial morphometry in granule cells. **(E-F)** Mitochondrial density, expressed as number of mitochondria per millimeter of granule cell, was assessed at P11 **(E)** (Sal-N versus Sal-Hx, *P=0.0279) and P45 **(F)** (Sal-N versus LPS-Hx, *P= 0.0340; LPS-N versus LPS-Hx: **P=0.0040). **(G-H)** Mitochondrial surface area was quantified at P11 **(G)** (Sal-N versus Sal-Hx: **P=0.0139) and P45 **(H)** (Sal-N versus LPS-Hx, *P=0.0373). **(I-L)** Mitochondrial morphometry in Purkinje cells. **(I-J)** Mitochondrial density was assessed at P11 **(I)** and P45 **(J)**. (Sal-N versus LPS-Hx, *P = 0.0341) **(K-L)** Mitochondrial surface area was quantified at P11 **(K)** and P45 **(L). (M)** Representative electron micrographs illustrating mitochondrial ultrastructural quality assessment. A severity scoring system ranging from 1 (healthy matrix with aligned cristae, blue) to 5 (mitophagy with minimal cristae and large vacuoles, red) was applied. **(N-O)** Pie chart visualization of mitochondrial health distribution in granule cells **(N)** and Purkinje cells **(O)** across experimental groups at P11 and P45. For **(A)** n = 8-14 per group. For **(B)**, n = 5-6 per group; one-way ANOVA with Tukey's post hoc correction. For **(C)**, n = 4-6 per group; ANOVA on ranks with pairwise comparisons. For **(E)**, n = 16-21 per

group; one-way ANOVA with Tukey's post hoc correction. For **(F)**, n = 11-21 per group; one-way ANOVA with Tukey's post hoc correction. For **(G)**, n = 57-114 per group; Kruskal-Wallis test with Dunn's post hoc correction. For **(H)**, n = 41-77 per group; Kruskal-Wallis test with Dunn's post hoc correction. For **(I)**, n = 6-8 per group; one-way ANOVA with Tukey's post hoc correction. For **(J)**, n = 3-8 per group; one-way ANOVA with Tukey's post hoc correction. For **(K)**, n = 669-757 per group; Kruskal-Wallis test with Dunn's post hoc correction. For **(L)**, n = 528-1783 per group; Kruskal-Wallis test with Dunn's post hoc correction. Data are presented as mean ± SD; *P < 0.05, **P < 0.01, ****P < 0.0001. EM, electron microscopy; FCCP, carbonyl cyanide-p-trifluoromethoxyphenylhydrazone; GC, granule cell; Hx, hypoxia; LPS, lipopolysaccharide; N, normoxia; PC, Purkinje cell; Sal, saline; SD, standard deviation.

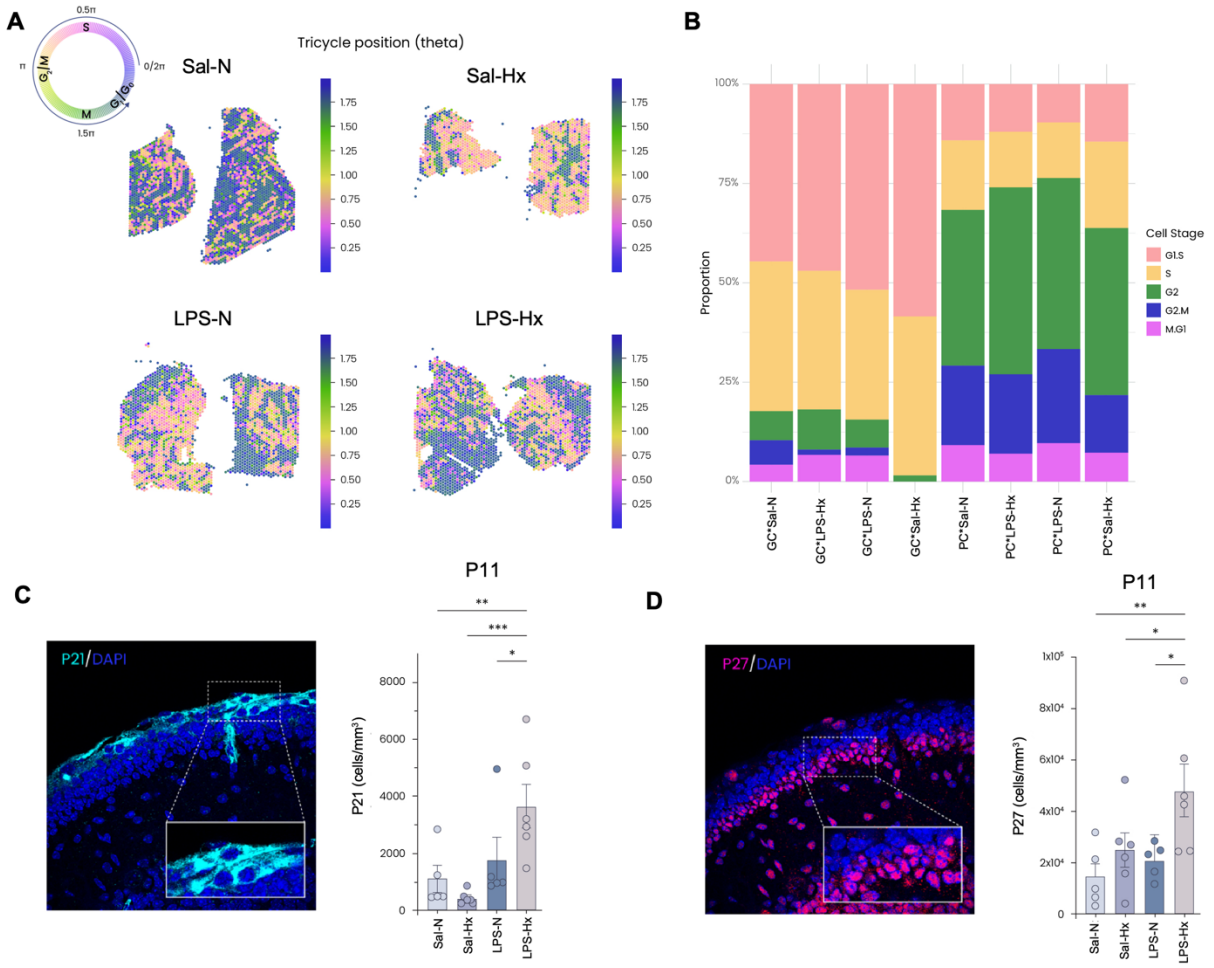

Figure 5 - MIA Differentially Reconfigures Hx-Induced Alterations in Neuronal Cell Cycle Dynamics: (A) Spatial mapping of cell cycle phase distribution in mouse cerebellum. Top left schematic illustrates the cell cycle phases corresponding to the theta value with associated color scale: G1/G0 phase (blue/purple, θ < 0.25 and θ > 1.75), S phase (pink to yellow, θ = 0.5-1.0), and G2/M phase (green, θ = 1.25-1.75). Representative spatial transcriptomics images display cell-cycle phase distribution across cerebellar tissue for each experimental group. **(B)** Quantification of cell cycle phase proportions in granule cells and Purkinje cells across

experimental groups. Stacked bar graphs display the percentage of cells in each cell-cycle phase, with colors corresponding to phases indicated in the legend. **(C)** Immunofluorescent detection of the cell-cycle inhibitor p21 in mouse cerebellar tissue. Left panel shows representative 60× magnification image of p21 (cyan) and DAPI (blue) staining. Right panel displays quantification of p21-positive cells expressed as cells per cubic millimeter (Sal-N versus LPS-Hx, **P = 0.0070; LPS-N versus LPS-Hx, *P = 0.0388; Sal-Hx versus LPS-Hx, ***P = 0.0008). **(D)** Immunofluorescent detection of the cell cycle inhibitor p27 in mouse cerebellar tissue. Left panel shows representative 60× magnification image of p27 (magenta) and DAPI (blue) staining. Right panel displays quantification of p27-positive cells expressed as cells per cubic millimeter (Sal-N versus LPS-Hx, **P = 0.0042; LPS-N versus LPS-Hx, *P = 0.0160; Sal-Hx versus LPS-Hx, *P = 0.0290). For **(C)** and **(D)**, n = 5-6 per group; one-way ANOVA with uncorrected Fisher's LSD. Data are presented as mean ± SD; *P < 0.05, **P < 0.01, ***P < 0.001. DAPI, 4′,6-diamidino-2-phenylindole; GC, granule cell; Hx, hypoxia; LPS, lipopolysaccharide; LSD, least significant difference; N, normoxia; PC, Purkinje cell; Sal, saline; SD, standard deviation.

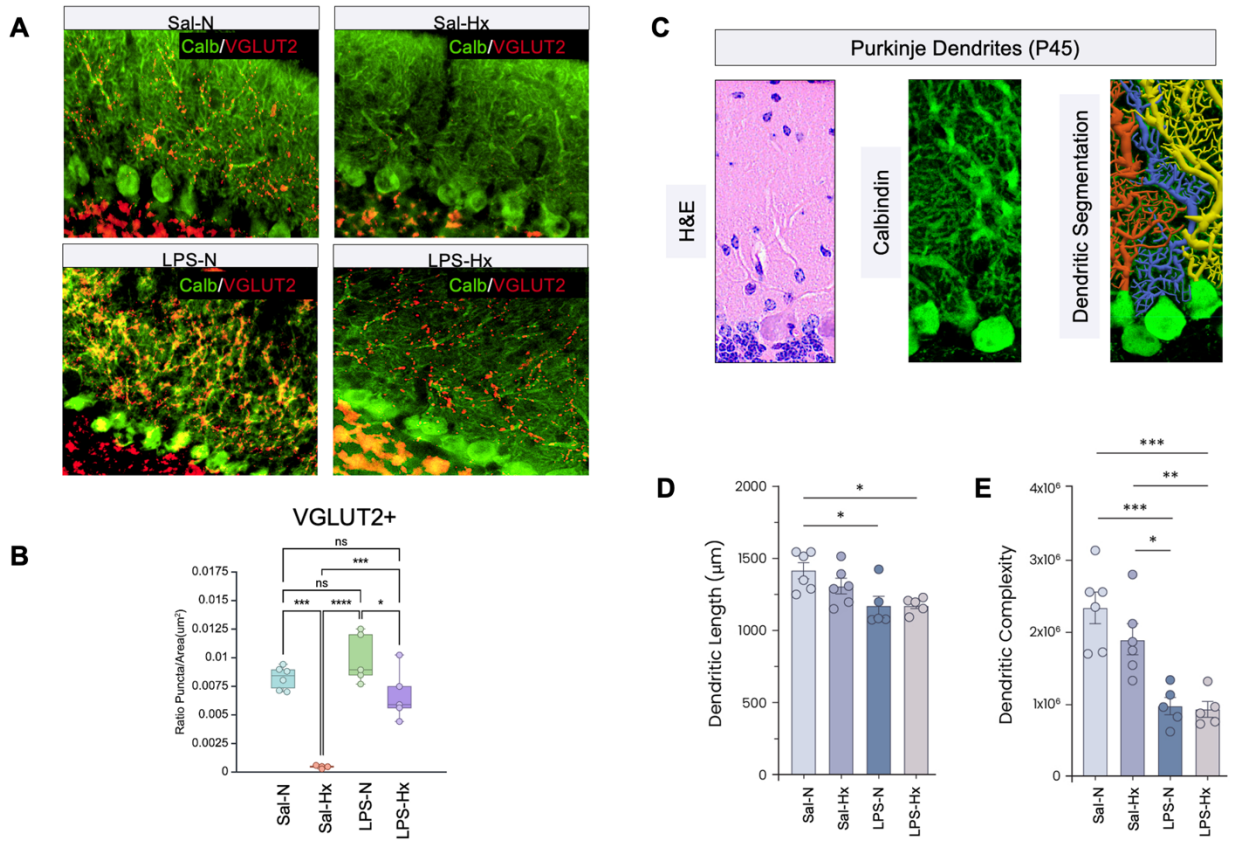

Figure 6 - Perinatal Insults Rewire the Cerebellar Connectome through Divergent Disruption of Cell-Cell Signaling Networks: (A) Representative confocal images of cerebellar tissue at 40× magnification displaying calbindin-immunostained Purkinje cells and dendrites (green) and VGLUT2-immunostained excitatory synaptic puncta (red). **(B)** Quantification of

excitatory synaptic density expressed as ratio of VGLUT2-positive puncta per area (Sal-N versus Sal-Hx, ***P < 0.001; Sal-Hx versus LPS-N, ****P < 0.0001; LPS-N versus LPS-Hx, *P = 0.0353). **(C)** Schematic illustration of the dendritic arborization quantification pipeline. Left panel displays hematoxylin and eosin-stained cerebellar section; middle panel shows representative calbindin-immunostained Purkinje cell imaged by confocal microscopy; right panel demonstrates user-guided dendritic tracing performed using Neurolucida 360 software. All images acquired at 40× magnification. **(D-E)** Quantification of Purkinje cell dendritic morphology at P45. Dendritic length **(D)** (Sal-N versus LPS-N, *P = 0.0233; Sal-N versus LPS-Hx, *P = 0.0256) and dendritic complexity **(E)** (Sal-N versus LPS-N, ***P = 0.0003; Sal-N versus LPS-Hx, ***P = 0.0002; Sal-Hx versus LPS-N, *P = 0.0114) were assessed across experimental groups. For **(B)** and **(D-E)**, n = 4-5 per group; one-way ANOVA with Tukey's post hoc correction. Data are presented as mean ± SD; *P < 0.05, ***P < 0.001, ****P < 0.0001. Calb, calbindin; GC, granule cell; H&E, hematoxylin and eosin; Hx, hypoxia; LPS, lipopolysaccharide; N, normoxia; PC, Purkinje cell; Sal, saline; SD, standard deviation; VGLUT2, vesicular glutamate transporter 2.

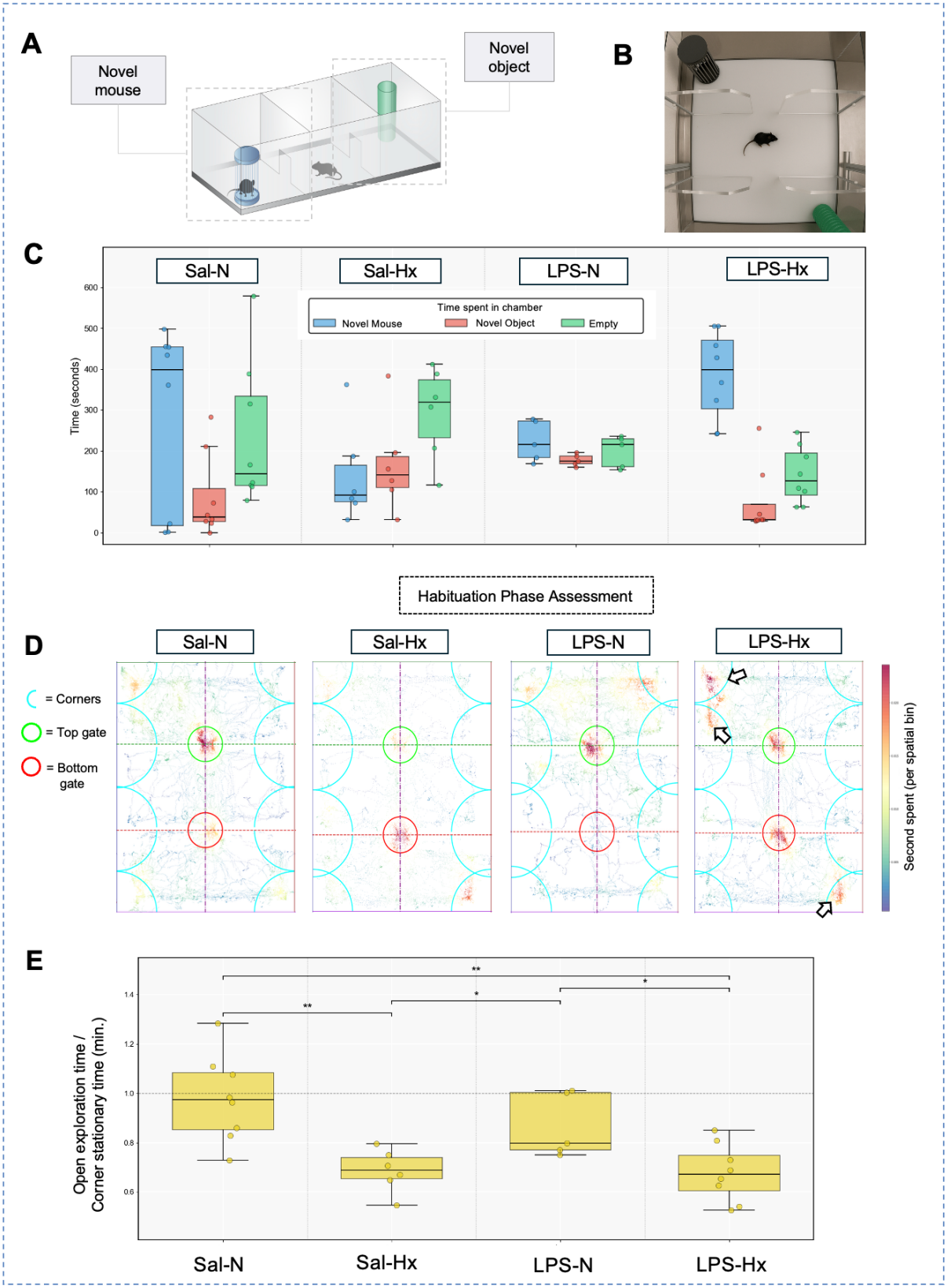
A
Novel mouse
Novel object
B
C
Sal-N
Sal-Hx
LPS-N
LPS-Hx
Time spent in chamber
Novel Mouse
Novel Object
Empty
Time (seconds)
Habituation Phase Assessment
D
= Corners
= Top gate
= Bottom gate
Second spent (per spatial bin)
E
Open exploration time / Corner stationary time (min.)

Figure 7 - MIA and Hx Elicit Divergent Social and Exploratory Phenotypes: (A) Schematic illustration of the three-chambered social approach assay used to evaluate sociability in mice. Left chamber contains an unfamiliar stimulus mouse housed within a cylindrical wire cage; middle chamber represents the arena where the test subject is placed; right chamber contains a novel object (green cylinder). **(B)** Photographic illustration of the experimental apparatus displaying the three-chamber configuration. **(C)** Quantification of time spent in each chamber across experimental groups. Blue boxplots represent time spent in the novel mouse chamber, red boxplots represent time spent in the novel object chamber, and green boxplots represent time spent exploring other areas within the arena. **(D)** Representative movement traces from individual mice during the habituation phase (stimuli-free) assessment. Tracked trajectories are displayed for each experimental group, with chamber corners demarcated by light blue semicircles, top gate area indicated in green, and bottom gate area indicated in red. Horizontal red and green lines mark chamber boundaries; vertical purple line represents the chamber midline. Heatmap scale indicates time spent per spatial bin ranging from 0.01 seconds (blue) to 0.06 seconds (red). **(E)** Quantification of exploratory behavior expressed as the ratio of open exploration time to corner stationary time across experimental groups. Horizontal dashed line indicates a balanced ratio (ratio = 1) (Sal-N versus Sal-Hx, **P = 0.002; Sal-N versus LPS-Hx, **P = 0.002; Sal-Hx versus LPS-N, *P = 0.03; LPS-N versus LPS-Hx, *P = 0.03). For **(C)**, n = 6-8 per group; between-group comparisons performed using one-way ANOVA with Welch's t-test; within-group comparisons performed using independent samples t-test. For **(E)**, one-way ANOVA with Tukey's post hoc correction. Data are presented as mean ± SEM **(C)** or mean ± SD **(E)**; *P < 0.05, **P < 0.01, ***P < 0.001. Hx, hypoxia; LPS, lipopolysaccharide; N, normoxia; Sal, saline; SD, standard deviation; SEM, standard error of the mean.

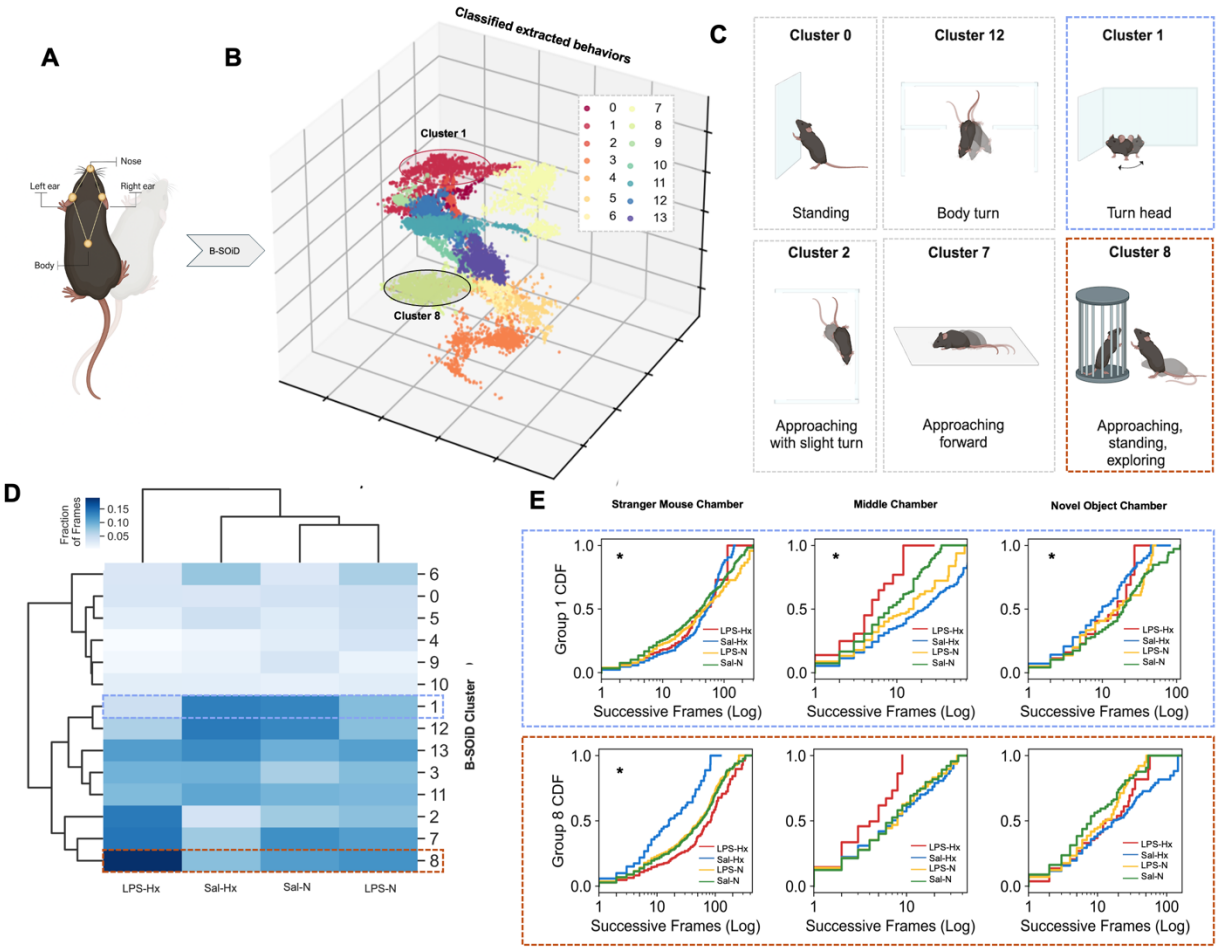

Figure 8 - MIA Pre-Exposure Shifts Hx-Induced Motor Stereotypies toward Heightened Social Behavior: (A) Schematic illustration of body point tracking for kinematic analysis. Anatomical landmarks including nose, left ear, right ear, and body center were identified and tracked to capture mouse movement during behavioral testing. **(B)** Three-dimensional visualization of the 14 kinematic behavioral clusters identified by the B-SOiD (Behavioral Segmentation of Open-field In DeepLabCut) algorithm. B-SOiD is an unsupervised machine-learning tool that classifies high-resolution kinematic data into distinct behavioral patterns based on movement motifs. Clusters 1 and 8 are highlighted as regions of interest. **(C)** Representative illustrations depicting a sample of the kinematic motifs associated with selected behavioral clusters. Cluster 0, standing; Cluster 12, body turn; Cluster 1, turn head; Cluster 2, approaching with slight turn; Cluster 7, approaching forward; Cluster 8, approaching, standing, and exploring. **(D)** Heatmap displaying the frequency of kinematic motifs across experimental groups, expressed as fraction of video frames classified into each of the 14 behavioral clusters.

Color intensity ranges from light blue (lower fraction) to dark blue (higher fraction). Hierarchical clustering dendrogram illustrates group relationships based on behavioral similarity. Brackets indicate group pairings for statistical comparisons. **(E)** Cumulative distribution function plots displaying the duration of behavioral bouts for Cluster 1 (top row) and Cluster 8 (bottom row) across the three chambers (stranger mouse chamber, middle chamber, and novel object chamber). Duration is expressed as successive frames on a logarithmic scale. Asterisks indicate comparisons with at least one statistically significant interaction. Analysis statistical details in Supplemental File. For **(D-E)**, n = 3-10 per group; Wasserstein distance with Benjamini-Hochberg correction applied to P-values. B-SOiD, Behavioral Segmentation of Open-field In DeepLabCut; CDF, cumulative distribution function; Hx, hypoxia; LPS, lipopolysaccharide; N, normoxia; Sal, saline.

A

Two-way RM ANOVA	SS	DF	MS	F (DFn	DFd)	P value
Sessions x Condition	1696435	49	34621	F (49	336) = 4.444	P<0.0001
Sessions	1245464	7	177923	F (7	336) = 22.84	P<0.0001
Condition	1374825	7	196404	F (7	48) = 11.54	P<0.0001
Subject	817223	48	17025	F (48	336) = 2.185	P<0.0001
Residual	2617723	336	7791			

Post-perturbation step-time

#	Tukey's multiple comparisons test	Predicted (LS) mean diff.	95.00% CIs	Summary	Adjusted P Value
5	Sal-N Post-perturbation vs. LPS-Hx Post-perturbation	-366.1	-514.9 to -217.2	****	<0.0001
5	Sal-N Post-perturbation vs. LPS-N Post-perturbation	-219.8	-368.6 to -70.90	***	0.0002
5	Sal-N Post-perturbation vs. Sal-Hx Post-perturbation	-186.6	-335.4 to -37.71	**	0.0038

B

Two-way RM ANOVA	SS	DF	MS	F (DFn	DFd)	P value
Sessions x Condition	623.3	21	29.68	F (21	168) = 1.694	P=0.0359
Sessions	878.3	7	125.5	F (7	168) = 7.161	P<0.0001
Condition	283.5	3	94.49	F (3	24) = 0.9169	P=0.4476
Subject	2473	24	103.1	F (24	168) = 5.881	P<0.0001
Residual	2944	168	17.52			

Missteps

#	Tukey's multiple comparisons test	Predicted (LS) mean diff.	95.00% CIs	Summary	Adjusted P Value
5	Sal-N vs. Sal-Hx	-10.03	-17.13 to -2.916	**	0.0019
5	LPS-N vs. Sal-Hx	-11.92	-19.87 to -3.970	***	0.0008
5	Sal-Hx vs. LPS-Hx	11.22	3.269 to 19.16	**	0.0019

Fig. S1: (A) Statistical output for post-perturbation step-time analysis. Top table displays two-way repeated-measures ANOVA results including sum of squares, degrees of freedom, mean square, F-statistic, and P-value for session × condition interaction, session main effect, condition main effect, subject variability, and residual variance. Bottom table presents Tukey's post hoc multiple comparisons test results for between-group differences at session 5, including predicted least squares mean differences, 95% confidence intervals, significance indicators, and adjusted

P-values. **(B)** Statistical output for misstep analysis. Top table displays two-way repeated-measures ANOVA results with corresponding statistical parameters. Bottom table presents Tukey's post hoc multiple comparisons test results for between-group differences at session 5. CI, confidence interval; DF, degrees of freedom; LS, least squares; MS, mean square; RM, repeated-measures; SS, sum of squares; #, ErasmusLadder session number.

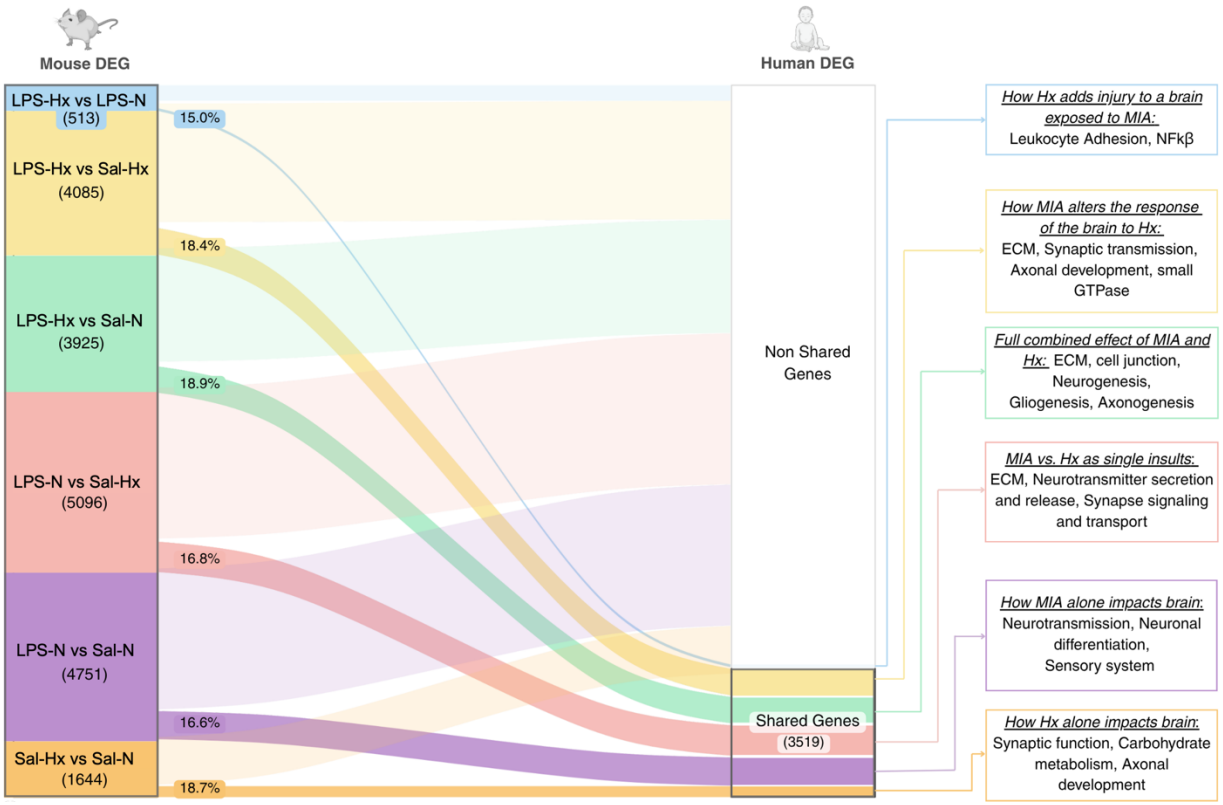

Fig. S2: Sankey diagram illustrating the overlap between differentially expressed genes identified in the sequential prematurity-associated insult mouse model and human preterm cerebellar tissue. Left panel displays pairwise comparisons between mouse experimental groups at P45, with the number of differentially expressed genes indicated below each comparison label. Colored ribbons represent shared genes between mouse comparisons and human preterm versus term cerebellar tissue, with percentages indicating the proportion of genes shared. Transparent ribbons indicate non-shared genes. Right panel displays color-coded boxes summarizing the top significantly enriched Gene Ontology-derived biological processes associated with each set of shared genes ($P < 0.05$). Enriched pathways include leukocyte adhesion and NFκB signaling

(hypoxia effects on maternal immune activation-exposed brain), extracellular matrix remodeling, synaptic transmission, axonal development, and small GTPase activity (maternal immune activation effects on brain response to hypoxia), as well as neurogenesis, gliogenesis, and axonogenesis (combined insult effects). For human studies, n = 4 per group; for mouse studies, n = 7 per group. DEG, differentially expressed genes; ECM, extracellular matrix; GO, Gene Ontology; GTP, guanosine triphosphate; Hx, hypoxia; LPS, lipopolysaccharide; N, normoxia; NFκB, nuclear factor kappa-light-chain-enhancer of activated B cells; Sal, saline.

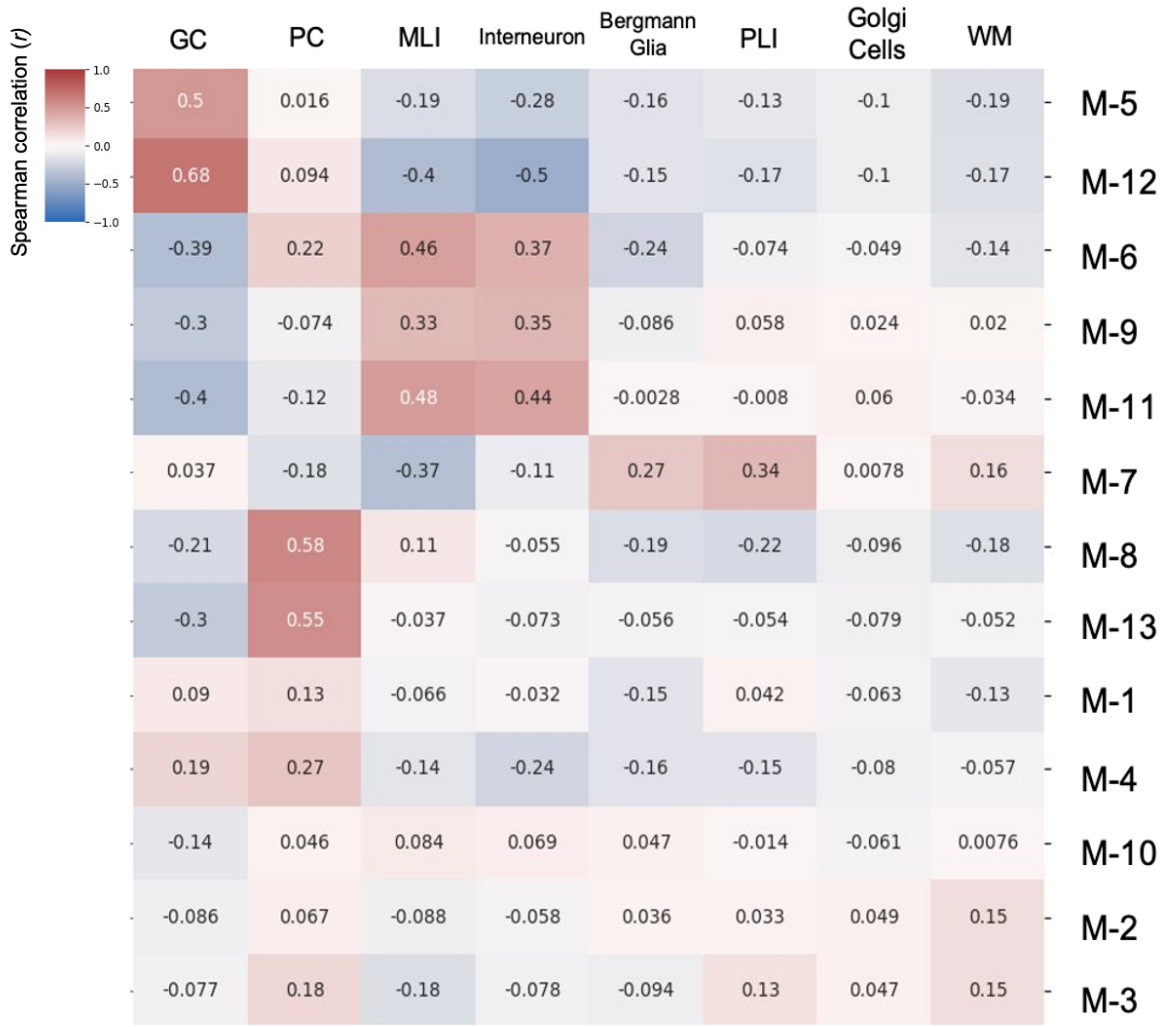

Fig. S3: Heatmap displaying Spearman correlation coefficients between mouse CoGAPS-derived expression patterns (M-1 through M-13) and cerebellar cell populations including granule cells, Purkinje cells, molecular layer interneurons, interneurons, Bergmann glia, Purkinje layer interneurons, Golgi cells, and white matter. Correlation values range from high positive (red, $r = 1$) to high negative (blue, $r = -1$). Patterns demonstrate cell-type-specific enrichment, with several patterns showing preferential correlation with granule cell or Purkinje cell populations. For all analyses, $n = 2$ per group. CoGAPS, Coordinated Gene Activity in Pattern Sets; GC, granule cell; Hx, hypoxia; LPS, lipopolysaccharide; M, mouse; MIA, maternal immune activation; MLI, molecular layer interneuron; N, normoxia; NES, normalized enrichment score; PC, Purkinje cell; PLI, Purkinje layer interneuron; Sal, saline; WM, white matter.

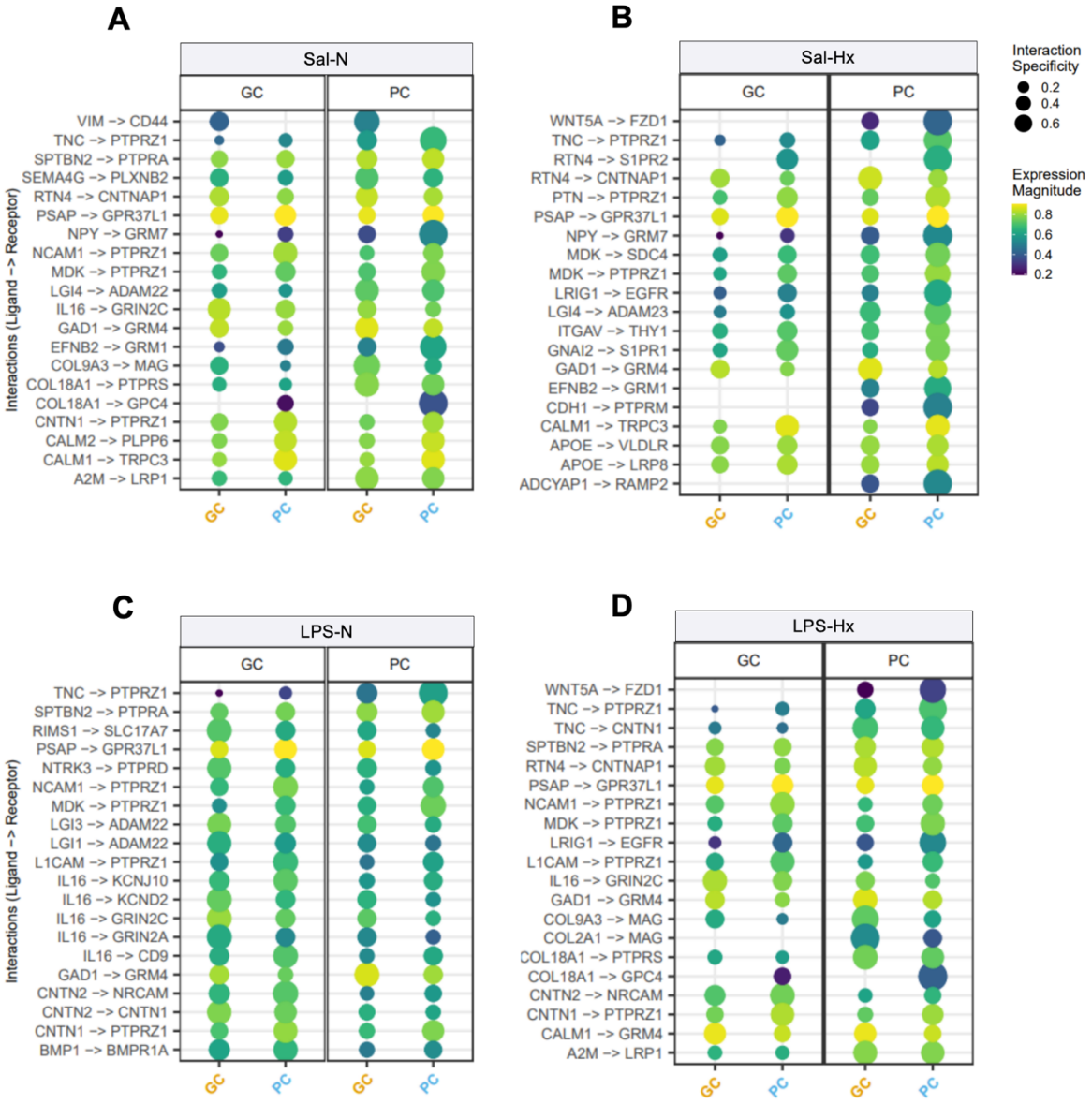

Fig. S4: (A-D) LIANA (LIgand-receptor ANalysis frAmework) plots displaying the top 20 predicted ligand-receptor interactions for each experimental group: Sal-N **(A)**, Sal-Hx **(B)**, LPS-N **(C)**, and LPS-Hx **(D)**. Interactions are shown between granule cell-granule cell (GC-GC), granule cell-Purkinje cell (GC-PC), Purkinje cell-Purkinje cell (PC-PC), and Purkinje cell-granule cell (PC-GC) pairs. Circle size represents interaction specificity, ranging from 0.2 (small) to 0.6 (large). Color intensity represents expression magnitude, ranging from 0.2 (blue, low) to 0.8 (yellow, high). Dashed line boxes highlight predicted interactions related to glutamatergic signaling and synaptic transmission pathways. GC, granule cell; Hx, hypoxia;

LIANA, LIgand-receptor ANalysis frAmework; LPS, lipopolysaccharide; N, normoxia; PC, Purkinje cell; Sal, saline.

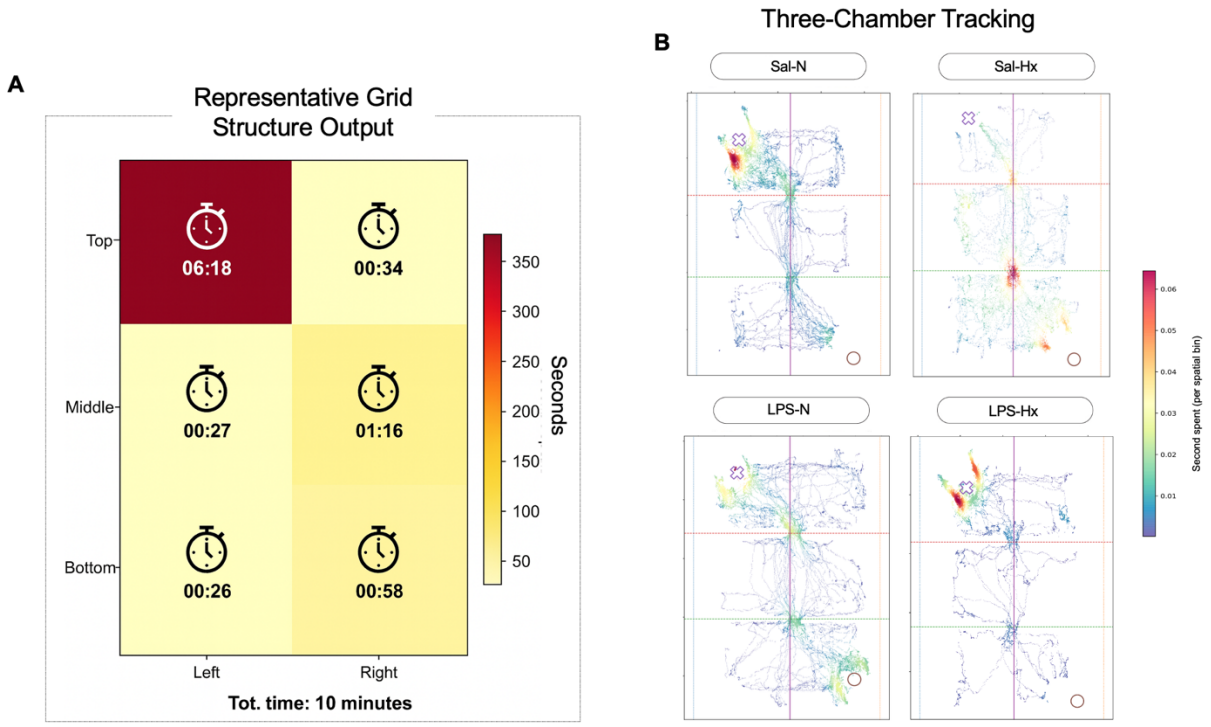

Fig. S5: (A) Representative schematic of the six-grid spatial analysis displaying time distribution across arena regions. The arena was divided into a 2 × 3 grid (top, middle, bottom rows; left and right columns), with time spent in each grid region indicated both by color intensity ranging from 50 seconds (yellow) to 350 seconds (red) and by actual time shown as minute:seconds below clock icon. **(B)** Representative movement tracking schematics for the three-chamber social approach assay across experimental conditions. Stranger mouse location is indicated by an x-symbol; novel object location is indicated by a circle-symbol. Dashed lines represent chamber boundaries. Color scale indicates time spent per spatial bin ranging from 0.005 seconds (blue) to 0.020 seconds (red).

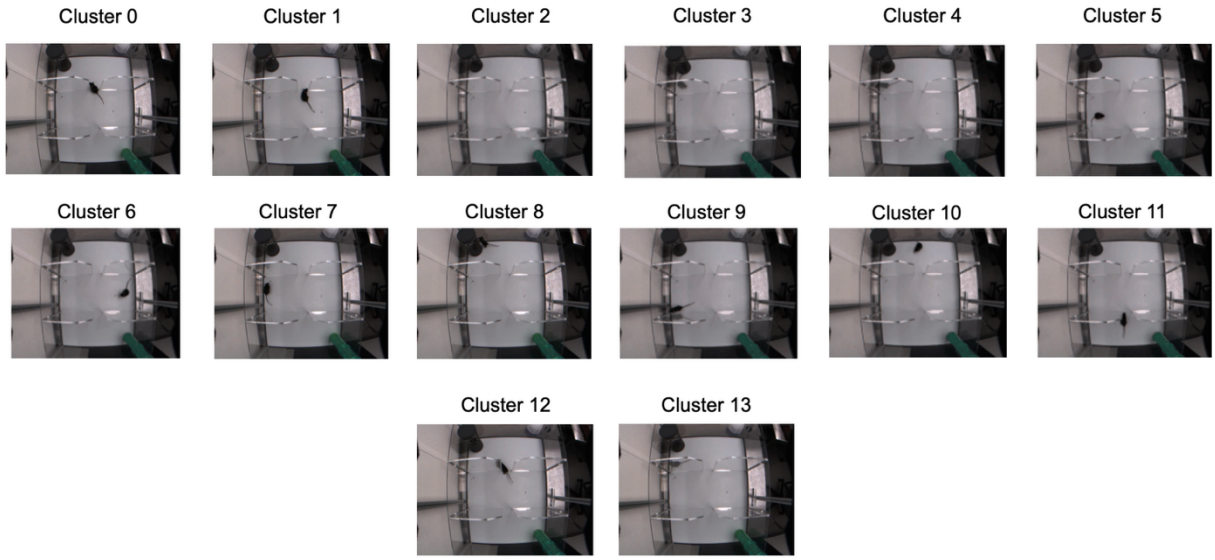

Fig. S6: Representative still frames from video segments illustrating the 14 distinct kinematic clusters (Clusters 0-13) identified by the B-SOiD algorithm. Each frame exemplifies a characteristic locomotor motif corresponding to a specific data-driven behavioral cluster extracted from high-resolution movement tracking during the three-chamber social approach assay. B-SOiD, Behavioral Segmentation of Open-field In DeepLabCut.

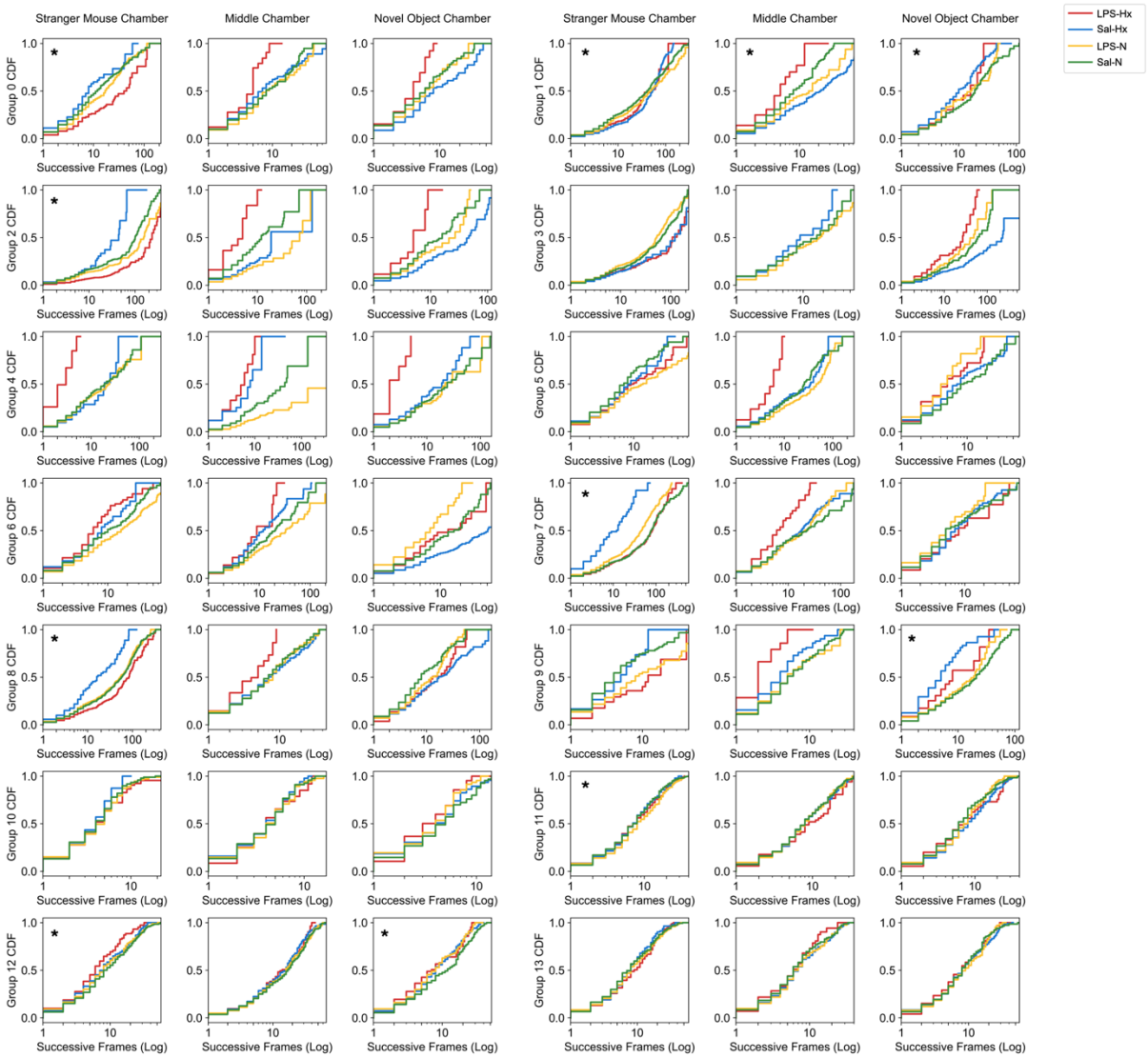

Fig. S7: Cumulative distribution function plots displaying the duration of behavioral bouts for all 14 kinematic clusters (Clusters 0-13) across the three chambers (stranger mouse chamber, middle chamber, and novel object chamber) for each experimental group. Duration is expressed as successive frames on a logarithmic scale (x-axis), with cumulative distribution function values on the y-axis. Each row represents a distinct kinematic cluster, and each column represents a chamber location. Line colors indicate experimental groups: Sal-N (green), Sal-Hx (yellow), LPS-N (blue), and LPS-Hx (red). Asterisks indicate comparisons with at least one statistically significant interaction between groups. For all analyses, n = 3-10 per group; Wasserstein distance with Benjamini-Hochberg correction applied to P-values. CDF, cumulative distribution function; Hx, hypoxia; LPS, lipopolysaccharide; N, normoxia; Sal, saline.

Table 1 - Demographic and Clinical Characteristics of preterm and term human subjects included in the transcriptomics analysis.

Variable	Term, n=4			Preterm, n=4		
	Mean ± SD	n	%	Mean ± SD	n	%
Sex						
Female		3	75		3	75
Male		1	25		1	25
Race						
Black		2	50		4	100
White		2	50		0	0
Ethnicity						
Hispanic or Latino		1	25		0	0
Not Hispanic or Latino		2	50		3	75
Unknown		1	25		1	25
GA (weeks)	40±0			26.4±0.5		
Postmenstrual age (weeks)	46±9.3			27.1±1		
Brain Weight (g)	435.5±82.8			305.7±15.6		

a. Abbreviations: GA, Gestational age

Table 2 - Demographical and Clinical Characteristics of human preterm subjects included in the transcriptomics analysis.

Subject ID	GA (weeks)	Postmenstrual age (weeks)	Sex	Brain Weight (g)	Race	Ethnicity	COD
Preterm 1	26.4	27	F	116.8	B	NH	Prematurity, Bowel perforation
Preterm 2	26	26.1	F	121.5	B	UK	Prematurity, ELBW
Preterm 3	27.3	28.7	F	154.5	B	NH	Prematurity, RDS, Intrauterine fetal hemorrhage
Preterm 4	26	26.4	M	830	B	NH	Bronchopneumonia

a. Abbreviations: B, Black; COD, Cause of death; ELBW, Extremely low birth weight; F, Female; GA, Gestational age; M, Male; NH, Non-Hispanic; UK, Unknown; RDS, Respiratory distress syndrome

Table 3 - Demographical and Clinical Characteristics of human term subjects included in the transcriptomics analysis.

Subject ID	GA (weeks)	Postmenstrual age (weeks)	Sex	Brain Weight (g)	Race	Ethnicity	COD
Term 1	40	40.7	F	404.5	W	UK	Sepsis, Coagulopathy, Multi-organ system failure
Term 2	40	41	F	404.3	B	NH	HSVII
Term 3	40	62.1	F	575	W	HL	Hypoplastic left ventricle, Double outlet right ventricle
Term 4	40	40.3	M	358	B	NH	CPT II deficiency

a. Abbreviations: B, Black; COD, Cause of death; F, Female; GA, Gestational age; HL, Hispanic Latino; M, Male; NH, Non-Hispanic; UK, Unknown; W, White, HSVII, Herpes simplex virus II

Table 4 – Kinematics behavioral cluster number and associated description.

Cluster	Kinematic Pattern	Locomotor Activity	Functional Label	Motif Description (spatially independent)	Attentional Load
0	Stationary, midline-oriented	Low	Pause / decision point	Mouse exhibits a complete cessation of movement with upright posture. Typically observed between transitions, this motif likely reflects a deliberative state or sensory sampling phase.	Very Low
1	Curved body, turning motion	Moderate	Directional reorientation	Mouse displays a curved body axis with asymmetric limb movement, indicative of an active turning maneuver redirecting its trajectory.	Moderate
2	Linear forward locomotion	High	Sustained movement	Mouse shows extended posture and forward stride, representing a canonical high-mobility	Low

				exploratory motif across the arena.	
3	Compact, angled posture	None	Investigatory fixation	Mouse maintains a close, crouched stance with its nose directed outward, reflecting a sensory investigation motif (e.g., sniffing or visual fixation).	High
4	Angled perimeter drift	Low	Scanning near edges	Mouse moves slowly along curved paths with partial orientation toward arena periphery. Reflects exploratory scanning or partial disengagement.	Moderate
5	Tucked posture, minimal movement	Very Low	Withdrawn / rest state	Mouse displays a compact, self-oriented stance with retracted head and little limb displacement. May represent behavioral reset or withdrawal.	Low
6	Oriented entry/exit posture	Moderate	Transitional boundary movement	Mouse exhibits directed locomotion toward or away from a zone boundary, often initiating or concluding chamber transitions.	High
7	Compact, static near stimulus	None	Sustained investigation	Mouse remains stationary with focused posture and sustained nose orientation, typically representing a prolonged interaction motif.	High
8	Static, corner-focused posture	None	Stimulus engagement (peripheral)	Mouse adopts a crouched position in a peripheral location with direct stimulus orientation, consistent with immersive inspection.	High
9	Elongated at directional transition	Moderate	Chamber entry/exit phase	Mouse exhibits forward movement with slight lateral reorientation, characteristic of directional transitions across zones.	Moderate-High
10	Stationary, stimulus-locked	None	High-attention fixation	Mouse remains immobile with nose and head oriented toward a stimulus, reflecting intensive sensory processing.	High
11	High-velocity forward drive	High	Fast traversal	Mouse moves in a straight path with increased speed, representing motivated arena-crossing behavior.	Low

12	Symmetrical forward motion	High	General exploration	Mouse displays balanced stride and straight posture, reflecting undirected but organized exploratory activity.	Low
13	Perpendicular stance at stimulus	None	High-intensity engagement	Mouse is oriented perpendicularly with a static body and focused attention, representing immersive investigatory behavior.	High